Theses and Dissertations

2008

Robust stabilization of resistive wall modes in Tokamak plasmas via [mu symbol]-synthesis

Joseph Delassio
Lehigh University

Follow this and additional works at: http://preserve.lehigh.edu/etd

Dalessio, Joseph

Robust Stabilization of Resistive Wall Modes in Tokamak Plasmas via μ-synthesis

January 2008

Robust Stabilization of Resistive Wall Modes

in Tokamak Plasmas via μ-synthesis

by

Joseph Dalessio

Presented to the Graduate and Research Committee of Lehigh University in

Candidacy for the Degree of Master of Science

in

Electrical Engineering

Lehigh University

Department of Electrical and Computer Engineering

Bethlehem, PA 18015

December 7, 2007

Certificate of Approval

This thesis is accepted and approved in partial fulfillment of the requirements for the Master of Science in Electrical Engineering.

_____December 7, 20007_____

Date

<div align="right">

_____

Professor Eugenio Schuster

Thesis Advisor

_____

Professor Svetlana Tatic-Lucic

Co-Advisor

_____

Professor Yujie Ding

Chairperson of Department

</div>

Acknowledgements

First, I would like to thank my advisor, Professor Eugenio Schuster, who gave me direction on countless occassions and without whom I would not have had the opportunity to do research in such an exciting field. I also want to thank him for providing me the opportunity to work at DIII-D with General Atomics in San Diego, CA over the summer of 2007. On that note, I would like to thank General Atomics; specifically David Humphreys, Michael Walker, and Anders Welander, for their assistance both research and non-research related during my summer stay. Also, Yongkyoon In of Fartech Inc. who provided the mathematical models and helping me understand plasma physics. Thanks also go out to my summer roommates Yongsheng Ou, Chao Xu, and David Sondak who all played a big part in the best summer of my life.

Most importantly, I would like to thank my parents, Fred and Arlene, my brother Jason and sister Nicole, and rest of my family for their continued support of my educational development.

Contents

List of Tables

List of Figures

Abstract

The control of the resistive wall mode (RWM) instability is one of the main areas of research at the DIII-D tokamak. The resistive wall mode is an instability caused by a kink in the plasma. Using the Far-Tech DIII-D/RWM model, which takes advantage of the resistive wall mode dynamics acting similar to a toroidal current sheet, a linear state space representation is considered. The states of the model are the currents in the walls of the tokamak and in the control coils surrounding the tokamak, which are used to stabilize the RWM. There are 12 internal feedback control coils and 3 external feedback control coils. Using a quadrature configuration to lock the internal feedback coils in amplitude and phase and ignoring the slow response of the external feedback coils, the effective number of inputs in the model is reduced to 3. The outputs are 22 magnetic field sensors composed of poloidal probes and saddle loops. These outputs are augmented with a matched filter to reduce the number of outputs to 2, representing the two orthogonal components of the RWM. The major term driving the instability is the RWM growth rate γ which is a time-varying uncertain parameter. Taking advantage of the structure of the state matrices, the model is reformulated into a robust control framework, with the growth rate of the RWM modeled as an uncertain parameter.

The controller design technique of μ-synthesis is used stabilize the RWM. The design is a robust control technique that takes advantage of an uncertain parameter influencing a nominal plant. Since there doesn't exist an optimal method to design a μ-synthesis controller, the DK-iteration method is used to design a controller that stabilizes the system for a range of practical growth rates. In order to effectively compare the results of the DK-iteration, additional model based control techniques were used, including the LQG, $LQRY$, and NCF controller designs. Also, the model based controllers are compared to the perfermance based PD control design. A stability and performance range of γ is stated for each of the controllers, quantifying the benefits of model based controllers. Implications for experimental implementation and use are discussed.

1

Chapter 1

Introduction

1.1   Background

Nuclear fusion produces energy through fusing together the nuclei of two light hydrogen atom isotopes (deuterium and tritium). Such a process requires an extreme amount of temperature and pressure to occur, since the nuclei need to overcome the Coulomb barrier (both nuclei carry positive charges). The high-temperature hydrogen isotopes must exist in a plasma (ionized gas) state in order to sustain fusion reactions. The confinement of this plasma can be provided by a tokamak, which is a magnetic confinement device in the shape of a torus. While confinement of the fusion plasma has been achieved, there are many instabilities that limit the performance and cause the loss of the plasma [1].

1.2   Resistive Wall Mode

One of the major non-axisymmetric instabilities in tokamaks is the resistive wall mode (RWM), a form of plasma kink instability whose growth rate is moderated by the influence of a resistive wall [2]. In a kink mode, the entire plasma configuration deforms in a helically symmetric manner with an extremely fast growth time (a

few microseconds) generating moving magnetic fields as it deforms that induce eddy currents in the surrounding conductive structure of the tokamak. These induced currents, in turn, generate magnetic fields that oppose the plasma deformation slowing the overall growth rate of the instability (to a few milliseconds), which enables the use of feedback to control the RWM. At present, current efforts focus on the stabilization of the $n = 1$ mode (the plasma perturbation repeats only once as the toroidal angle varies from 0 to 2π) because this instability is the first to occur when pressure rises.

The rise of pressure is characterized through the variable β, which collects key performance parameters of the plasma. The variable β provides a ratio between the internal kinetic pressure of the plasma and the external pressure of the magnetic field that confines the plasma [1] i.e.,

$$\beta = \frac{<P>}{\left[\frac{B_T^2}{2\mu_0}\right]}$$

where $<P>$ is the plasma kinetic pressure averaged over the plasma volume, B_T is the vacuum toroidal field strength, and μ_0 is the magnetic permeability of the vacuum. It is convenient to express this term as a normalized beta β_N such that

$$\beta_N = \frac{\beta}{\left[\frac{I_p}{aB_T}\right]}$$

where a is the plasma minor radius and I_p is the plasma current. Since the normalized beta β_N defines how much confining pressure is needed to maintain a given plasma pressure, it is a measure of efficiency of confinement. Magnetohydrodynamic theory predicts that when the surrounding wall structure is located far from the plasma surface, a sufficiently high plasma pressure will make the RWM unstable. Thus if a perfectly conducting wall is within a critical distance of the plasma, the unstable eigenmode could be stabilized by the mode-induced eddy currents in the wall. A per-

3

fect conductor assumes no internal resistance and thus no decay of the eddy currents in the wall. However, these resistive behaviors exist in practice causing the RWM mode amplitude to grow at a rate fractional to that of the wall time constant. The range of interest for the control of the RWM is between the critical β value where the plasma becomes unstable without a perfectly conducting wall and the critical β where the RWM is unstable even with the perfectly conducting wall due to high plasma pressure. This is the range between the "no-wall beta limit" $\beta_{N,no-wall}$ and the "ideal-wall beta limit" $\beta_{N,ideal-wall}$. The normalized plasma pressure efficiency β_N is further normalized based on the limits of interest to form a new variable

$$ C_\beta = \frac{\beta_N - \beta_{N,no-wall}}{\beta_{N,ideal-wall} - \beta_{N,no-wall}} $$

where C_β is a measure of the stability of the plasma to resistive wall modes. For $C_\beta < 0$ the RWM is always stable and for $C_\beta > 1$ the plasma cannot be practically stabilized. The range of interest for control of the RWM is $0 < C_\beta < 1$. Further, there exists a relationship between the normalized measure of stability C_β and growth rate of the RWM γ. There are efforts to fully understand this relationship, yet typically the growth rate increases for increasing C_β [3].

The Far-Tech DIII-D/RWM model represents the plasma surface as a toroidal current sheet and represents the wall using an eigenmode approach [4]. The plasma surface and current sheet perturbations are equivalent in the sense that they both produce the same magnetic field perturbation. Observations from experiments show that the mode spatial structure remains unchanged. This spatial invariance is described as mode rigidity, which implies that the spatial distribution of current on the plasma surface and the wall remain intact while only their magnitudes change. Using the surface current representation of the mode, it is possible to construct a state-space model of the plant, whose states are the surrounding wall current, and

the external control coil currents. Since the plasma is represented as a single mode, and due to the rigidity assumption, the state space model is parameterized with a scalar coupling coefficient c_{pp}, which is directly related to the growth rate γ of the mode, and is expressed as an inductive circuit equation derived from Faraday's Law.

Although the plasma surface deformation cannot be directly measured in real time, the magnitude and phase of the deformation can be diagnosed from measurements by a set of 22 magnetic field sensors composed of poloidal probes and saddle loops. An array of 12 control internal feedback coils (I-coils) can then be used to return the plasma to its original axisymmetric shape. Fig. 1.1 shows the arrangement of coils and sensors. Using an estimator for the two orthogonal components of the assumed $n = 1$ mode pattern, the resultant plant can be constructed into a reduced form from the original 12 input, 22 output [6]. In particular, using a typical quartet configuration for the I-coils and matched filter, the plant can be simplified to a 3 input, 2 output system. The three inputs represent three I-coils that are not locked in phase by the quartet configuration. The matched filter reduces the 22 outputs to two outputs that represent the RWM mode vector of the sine and cosine components. These two outputs can be combined to express the output as a single signal composed of the RWM amplitude and toroidal phase [4].

1.3   Objective

The overall goal of this work is to take advantage of the developed model of the DIII-D tokamak plasma to design a model based feedback controller for the resistive wall mode. The major term driving the instability is the RWM growth rate γ which is an uncertain time-varying parameter. This parameter, in the form of the scalar coupling coefficient c_{pp}, is buried within the state space representation of the plasma and it must be extracted and separated from the nominal plant model in order to write the

5

model in a robust control framework. Once the uncertain parameter is extracted, a robust controller based on the structured singular value μ [10] is designed to stabilize the RWM instability over a certain range of the growth rate γ. The controller must achieve stability and performance requirements over a large range of growth rate values. This has the benefits of designing one constant controller that can stabilize the plasma RWM instability over the entire physical range of the uncertain time-varying growth rate. The robust μ-synthesis controller is compared with previously reported results and other controllers in stabilizing the RWM instability [13].
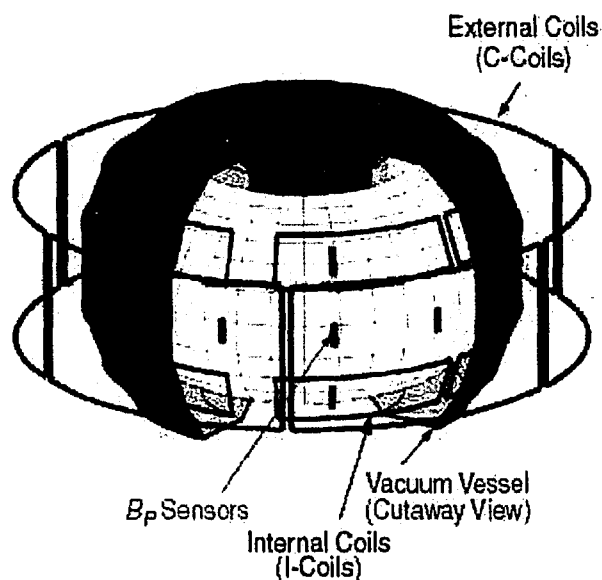
Figure 1.1: Coils and sensors for RWM magnetic feedback stabilization

Chapter 2

RWM Model

2.1 System Model

Stated below is the Far-Tech DIII-D/RWM model, a plasma response model for the resistive wall mode using a toroidal current sheet to represent the plasma surface [4]. Faraday's Law is used to derive the inductive circuit equation that describes the nonaxisymmetric plasma-conductor system

$$M_{ss}\dot{I}_s + R_{ss}I_s + \frac{\partial \psi_s}{\partial K_p}\dot{K}_p = V_s \tag{2.1}$$

where the subscript s represents the conductor (consisting of the wall and the coils) and the subscript p represents the plasma. The matrices M_{ss} is the mutual inductance between the vessel wall and the coils, R_{ss} is the resistance matrix, I_s is the current flowing in the conductor, V_s is the externally applied voltage to the conductor, $\frac{\partial \psi_s}{\partial K_p}$ is the change in flux at the conductors resulting from a modal amplitude proportional to K_p, where K_p is a mode amplitude parameterization function of applied flux at the plasma surface [5]. Using the assumption that

$$\frac{\partial \psi_s}{\partial K_p} = M_{sp} \tag{2.2}$$

7

where M_{sp} is the mutual inductance between either the wall or coils and the plasma and

$$K_p = C_{pp}\psi_p = C_{pp}\left(M_{ps}I_s\right) \tag{2.3}$$

where C_{pp} completely describes the energy source driving the instability, (2.2) and (2.3) can be substituted into (2.1). In general C_{pp} is a 2x2 matrix, which for the $n = 1$ RWM represents two degenerative (having the same growth rate) modes that allow the RWM to grow at any toroidal angle. It is possible for the two modes to have slightly different c_{pp} values due to the discreteness of the conductor model. The model under consideration has two modes influenced by the same growth rate, which results in the 2x2 C_{pp} matrix simplified to a scalar c_{pp}. This yields the system dynamics derived from Faraday's Law

$$(M_{ss} + M_{sp}c_{pp}M_{ps})\dot{I}_s + R_{ss}I_s = V_s.$$

The model is represented in terms of the couplings between the plasma (p), vessel wall (w), and coils (c). The mutual inductance matrices are given by

$$M_{ss} = \begin{bmatrix} M_{ww} & M_{wc} \\ M_{cw} & M_{cc} \end{bmatrix}, \; M_{sp} = \begin{bmatrix} M_{wp} \\ M_{cp} \end{bmatrix}, \; M_{ps} = \begin{bmatrix} M_{pw} & M_{pc} \end{bmatrix},$$

where M_{ps} and M_{sp} satisfy the following condition

$$M_{ps} = M_{sp}^T = \begin{bmatrix} M_{wp}^T & M_{cp}^T \end{bmatrix} \Rightarrow M_{pw} = M_{wp}^T, M_{pc} = M_{cp}^T.$$

The resistance matrix is given by

$$R_{ss} = \begin{bmatrix} \lambda_w & 0 \\ 0 & R_c \end{bmatrix},$$
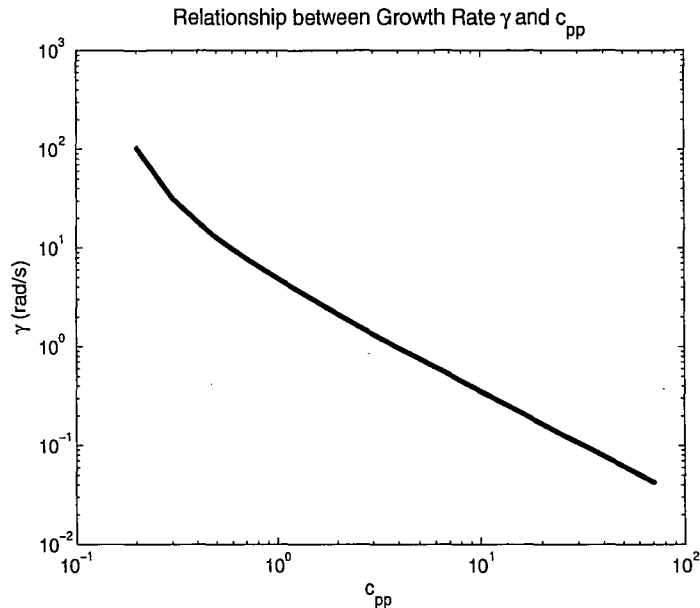
Figure 2.1: Empirical relationship between the growth rate γ and c_{pp}

where λ_w characterizes the couplings of a wall surface currents and R_c is the coil resistance. The conductor current and externally applied conductor voltage can be written as

$$I_s = \begin{bmatrix} I_w \\ I_c \end{bmatrix}, \quad V_s = \begin{bmatrix} 0 \\ V_c \end{bmatrix},$$

where I_w is the wall current, I_c is the coil current, and V_c is the externally applied voltage to the coil.

Most of the matrices and variables presented are characteristics of the tokamak and are well known. The uncertainty is introduced through the variable c_{pp}, which is based on the growth rate γ of the resistive wall mode. The relationship between these variables is shown empirically in Fig. 2.1 and is further explained in [6].

This model can be represented in a state space formulation using the conductor current as the state ($x = I_s$) and the applied voltage as the input ($u = V_s$). This results in the following state space equation

$$\dot{x} = Ax + Bu$$

9

where

$$A = -L_{ss}^{-1}R_{ss}, \qquad B = L_{ss}^{-1}, \qquad (2.4)$$

where $L_{ss} = M_{ss} - M_{sp}c_{pp}M_{ps}$. The output equation of the state space representation is based on sensor measurements that relate to the coil current through the dynamics

$$y = (C_{ss} - C_{yp}c_{pp}M_{ps})I_s$$

where C_{yp} is the coupling matrix between the sensor and plasma current and

$$C_{ss} = \begin{bmatrix} C_{yw} & C_{yc} \end{bmatrix}$$

is given by the coupling matrix between the sensor and wall current C_{yw}, and the coupling matrix between the sensor and coil current C_{yc}. This results in the state space output equation

$$y = Cx$$

where

$$C = C_{ss} - C_{yp}c_{pp}M_{ps}. \qquad (2.5)$$

2.2   Model Transformation

2.2.1   Parameterization of the L_{ss}^{-1} Matrix

The goal is to extract c_{pp} from the uncertain state space system and introduce it as an uncertainty block that perturbs a nominal state space system. The initial step to obtaining the nominal state space system is to express each state matrix as a general state space representation affine in nonlinear functions of the uncertainty c_{pp}. As seen in (2.4), the majority of the complexity is introduced in the A and B state matrices, where the uncertainty c_{pp} is introduced through L_{ss}^{-1}, and where

$L_{ss} = (M_{ss} - M_{sp}c_{pp}M_{ps})$. Using the fact the c_{pp} is scalar and that the matrix product $M_{sp}M_{ps}$ is rank 2, the L_{ss} matrix can be expressed as

$$
\begin{aligned}
L_{ss} &= M_{ss} - M_{sp}c_{pp}M_{ps} \\
&= M_{ss} - c_{pp}M_{sp}M_{ps} \\
&= M_{ss} - c_{pp}\sum_{i=1}^{2} u_i u_i'
\end{aligned}
\tag{2.6}
$$

where

$$
M_{sp} = \begin{bmatrix} u_1 & u_2 \end{bmatrix}, \quad M_{ps} = \begin{bmatrix} u_1' \\ u_2' \end{bmatrix}
$$

where u_1 and u_2 are $n \times 1$ vectors, u_1' and u_2' are the transpose of u_1 and u_2 respectively and are $1 \times n$ vectors, and n is the number of states in the RWM state space model. To obtain a parameterized expression for the L_{ss}^{-1} term, we must first compute the inverse of a matrix sum. Given the matrix A_T, the scalar b_T, and the vectors C_T and D_T, the inverse of a matrix sum is given by the Sherman-Morrison formula as [7]

$$
(A_T - b_T C_T D_T)^{-1} = A_T^{-1} + \frac{b_T(A_T^{-1}C_T)(D_T A_T^{-1})}{1 - b_T D_T A_T^{-1} C_T}.
\tag{2.7}
$$

Using (2.6), the inverse of L_{ss} can be written as

$$
L_{ss}^{-1} = (M_{ss} - M_{sp}c_{pp}M_{ps})^{-1} = (M_{ss} - c_{pp}u_1 u_1' - c_{pp}u_2 u_2')^{-1}.
$$

Now, using the matrix $A_l = M_{ss} - c_{pp}u_1 u_1'$ the above equation can be written as

$$
L_{ss}^{-1} = (A_l - c_{pp}u_2 u_2')^{-1}.
$$

This is now in the form given by (2.7) and thus the formula can be applied, resulting in

$$L_{ss}^{-1} = A_l^{-1} + \frac{c_{pp}(A_l^{-1}u_2)(u_2'A_l^{-1})}{1 - c_{pp}u_2'A_l^{-1}u_2}. \tag{2.8}$$

Now the matrix L_{ss}^{-1} is expressed in terms of A_l^{-1}, which is equivalent to $(M_{ss} - c_{pp}u_1u_1')^{-1}$, and once again applying (2.7) results in

$$A_l^{-1} = (M_{ss} - c_{pp}u_1u_1')^{-1} = M_{ss}^{-1} + \frac{c_{pp}(M_{ss}^{-1}u_1)(u_1'M_{ss}^{-1})}{1 - c_{pp}u_1'M_{ss}^{-1}u_1}.$$

This expression can now be substituted back into (2.8), which yields

$$
\begin{aligned}
L_{ss}^{-1} = & M_{ss}^{-1} + \frac{c_{pp}(M_{ss}^{-1}u_1)(u_1'M_{ss}^{-1})}{1 - c_{pp}u_1'M_{ss}^{-1}u_1} + \frac{c_{pp}}{1 - c_{pp}u_2'(M_{ss}^{-1} + \frac{c_{pp}(M_{ss}^{-1}u_1)(u_1'M_{ss}^{-1})}{1-c_{pp}u_1'M_{ss}^{-1}u_1})u_2} * \\
& \left(M_{ss}^{-1} + \frac{c_{pp}(M_{ss}^{-1}u_1)(u_1'M_{ss}^{-1})}{1 - c_{pp}u_1'M_{ss}^{-1}u_1} \right) u_2u_2' \left(M_{ss}^{-1} + \frac{c_{pp}(M_{ss}^{-1}u_1)(u_1'M_{ss}^{-1})}{1 - c_{pp}u_1'M_{ss}^{-1}u_1} \right).
\end{aligned}
$$

Expanding the terms and factoring out the terms dependent on c_{pp}, the equation simplifies to

$$
\begin{aligned}
L_{ss}^{-1} = & M_{ss}^{-1} + \frac{c_{pp}}{1 - c_{pp}u_1'M_{ss}^{-1}u_1}(M_{ss}^{-1}u_1)(u_1'M_{ss}^{-1}) \\
& + \frac{c_{pp}}{1 - c_{pp}u_2'M_{ss}^{-1}u_2 - \frac{c_{pp}^2}{1-c_{pp}u_1'M_{ss}^{-1}u_1}u_2'(M_{ss}^{-1}u_1)(u_1'M_{ss}^{-1})u_2} \left\{ \left[(M_{ss}^{-1}u_2)(u_2'M_{ss}^{-1}) \right] \right. \\
& + \frac{c_{pp}}{1 - c_{pp}u_1'M_{ss}^{-1}u_1} \left[(M_{ss}^{-1}u_2) \left(u_2'(M_{ss}^{-1}u_1)(u_1'M_{ss}^{-1}) \right) \right. \\
& \hspace{6cm} \left. + \left((M_{ss}^{-1}u_1)(u_1'M_{ss}^{-1})u_2 \right) \left(u_2'M_{ss}^{-1} \right) \right] \\
& + \left(\frac{c_{pp}}{1 - c_{pp}u_1'M_{ss}^{-1}u_1} \right)^2 \left[(M_{ss}^{-1}u_1)(u_1'M_{ss}^{-1})u_2u_2'(M_{ss}^{-1}u_1)(u_1'M_{ss}^{-1}) \right] \right\}.
\end{aligned}
$$

The terms can be collected and rewritten in the form

$$B = L_{ss}^{-1} = \sum_{i=0}^{4} \alpha_i B_i,$$

where α_i's are nonlinear functions of c_{pp}, and B_i's are constant matrices. The individual terms are given by

$$
\begin{aligned}
\alpha_0 &= 1 \\
\alpha_1 &= \frac{c_{pp}}{1 - c_{pp} u_1' M_{ss}^{-1} u_1} \\
\alpha_2 &= \frac{c_{pp}}{1 - c_{pp} u_2' M_{ss}^{-1} u_2 - \frac{c_{pp}^2}{1 - c_{pp} u_1' M_{ss}^{-1} u_1} u_2' (M_{ss}^{-1} u_1)(u_1' M_{ss}^{-1}) u_2} \\
\alpha_3 &= \alpha_2 \alpha_1 \\
\alpha_4 &= \alpha_2 \alpha_1^2 \\
B_0 &= M_{ss}^{-1} \\
B_1 &= \left[(M_{ss}^{-1} u_1)(u_1' M_{ss}^{-1}) \right] \\
B_2 &= \left[(M_{ss}^{-1} u_2)(u_2' M_{ss}^{-1}) \right] \\
B_3 &= \left[(M_{ss}^{-1} u_2) \left(u_2' (M_{ss}^{-1} u_1)(u_1' M_{ss}^{-1}) \right) \right. \\
&\quad \left. + \left((M_{ss}^{-1} u_1)(u_1' M_{ss}^{-1}) u_2 \right) (u_2' M_{ss}^{-1}) \right] \\
B_4 &= \left[(M_{ss}^{-1} u_1)(u_1' M_{ss}^{-1}) u_2 u_2' (M_{ss}^{-1} u_1)(u_1' M_{ss}^{-1}) \right].
\end{aligned}
$$

2.2.2 Expressing the Parameterized State Space Matrices

The last section allowed us to express the L_{ss}^{-1} matrix in a parameterized form, which allows the parameterization of the state and input matrices A and B respectively. In a similar way, the output matrix C can also be parameterized. Using the fact that c_{pp} is a scalar, the C matrix can be written as

$$
C = C_{ss} - C_{yp} c_{pp} M_{ps} = C_{ss} - c_{pp} C_{yp} M_{ps} = C_0 + \alpha_5 C_5,
$$

where

$$
C_0 = C_{ss}, \quad C_5 = -C_{yp} M_{ps}, \quad \alpha_5 = c_{pp}.
$$

Defining $A_i = -B_i R_{ss}$, we can finally summarize the parameterized expressions for the state matrices A, B, and C in terms of α_i's, given as

$$A = A_0 + \alpha_1 A_1 + \alpha_2 A_2 + \alpha_3 A_3 + \alpha_4 A_4 \tag{2.9}$$

$$B = B_0 + \alpha_1 B_1 + \alpha_2 B_2 + \alpha_3 B_3 + \alpha_4 B_4 \tag{2.10}$$

$$C = C_0 + \alpha_5 C_5. \tag{2.11}$$

2.2.3 Behavior of Nonlinear Uncertainties

With the creation of five new variables that all depend on c_{pp}, it is important to study the behavior of these variables with respect to our uncertainty c_{pp}. The range considered for c_{pp} is determined by the growth rate of the resistive wall mode and by the number of eigenmodes used in the model. A thorough comparison of the number eigenmodes needed to fully represent the resistive wall mode is explained in [6]. This comparison determined that using 15 or 29 eigenmodes have similiar results and are the best representation of the resistive wall mode. The number of eigenvalues (or states) for a given eigenmode model is determined by double number of eigenmodes (due to the quadrature relationship of the wall currents) and the number of control coils currents. There are 6 control coil currents, 3 of which are due to the slower external feedback coils (C-coils) and the remaining 3 are due to the internal feedback coils (I-coils). It was found in [8] that the I-coils are much more effective at controlling the RWM than the slower C-coils. For this reason, the controller design is based on 3 inputs (I-coils), however the C-coil currents remain in the model for the determination of the number of eigenvalues. Using a physically realizable growth rate γ range from 10 rad/s to 5,000 rad/s, the corresponding c_{pp} range for the 29 eigenmode and 15 eigenmode model is given by 71 to 0.3325. The 29 eigenmode model of the DIII-D tokamak, RWM model is defined with 3 inputs, 23 outputs, and 67 states, while the 15

14

eigenmode model has 3 inputs, 23 outputs, and 36 states. As seen earlier, the variable α_5 is directly equal to the uncertainty c_{pp} thus rendering a linear relationship. This trivial case is not plotted to emphasize the nonlinearities in the first four variables. As seen in Fig. 2.2, the variables α_1 and α_2 are approximately equal to each other, with a maximum error on the order of 10^{-6}. Also note that except for high growth rates, which correspond to small c_{pp} values, the α parameters are approximately constant. This approximately constant behavior is valid for c_{pp} values larger than 3. Although the state matrices are expressed in a linear form, the coefficients of each individual state matrix components are clearly nonlinear, which calls for additional manipulation to conform to a parameterized robust control framework.
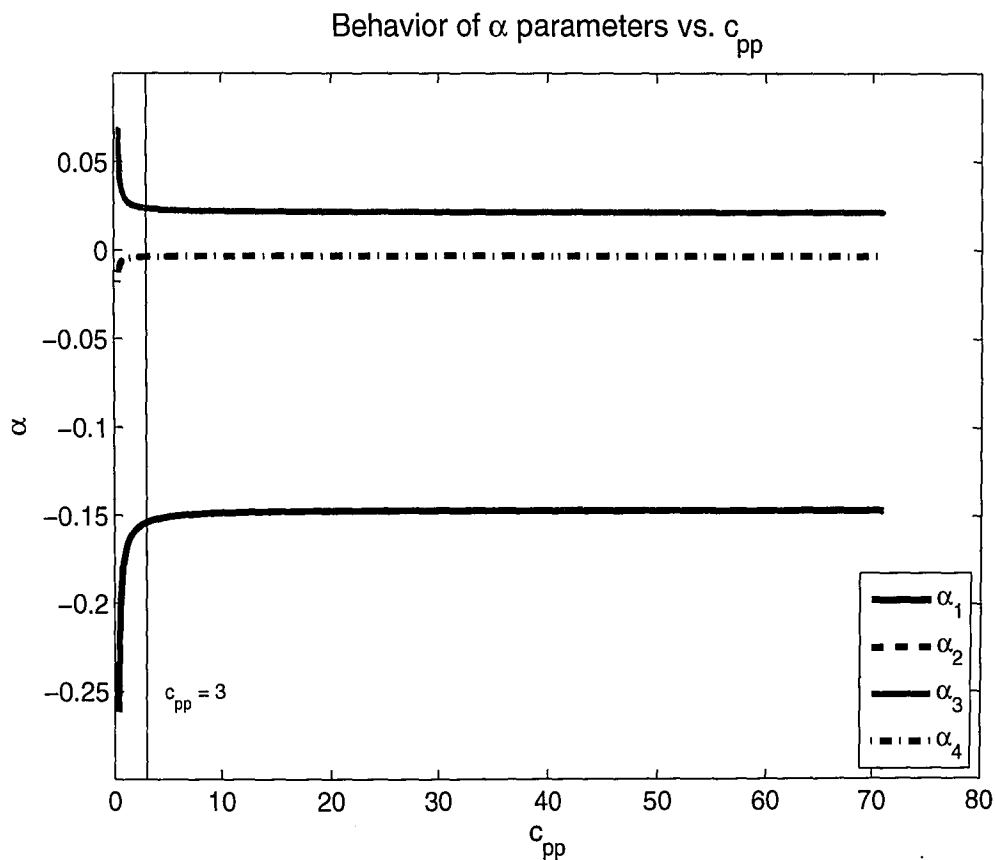

Figure 2.2: Nonlinear Uncertainties (α_i) versus c_{pp}

2.2.4 Behavior of System's Unstable Eigenvalue

With the introduction of new matrices and nonlinear uncertainties, it is important to examine the behavior of the system to ensure that the new representation complies with the original system dynamics. In particular, the system characteristic of most importance in the unstable eigenvalue behavior that varies with the uncertainty c_{pp}. Using the newly developed representation of the state matrices given by (2.9)-(2.11), the system's unstable eigenvalue for the 29 eigenmode model is plotted in Fig. 2.3.

The figure is plotted over the same uncertainty range previously defined for c_{pp}. The behavior of the unstable eigenvalue is consistent with the expected system dynamics. At faster RWM growth rates (smaller c_{pp}) the system is much more unstable than the slower RWM growth rates. When the working range of c_{pp} is relaxed, the 29 eigenmode model produces a singularity at $c_{pp} = 0.1521$. This value is comparable with the c_{pp} value of 0.1519 presented in [6].

2.3 Growth Rate Parameterization

In order to represent the uncertain state space matrix in conventional $M\Delta$ formulation for the robust control framework, several intermediary steps must be performed. First of all, the state space realization of the system transfer function using linear fractional transformation must be developed.

2.3.1 Definition of Linear Fractional Transformation

Linear fractional transformation (LFT) is a matrix function convenient for formulating control problems. Given a complex partitioned matrix

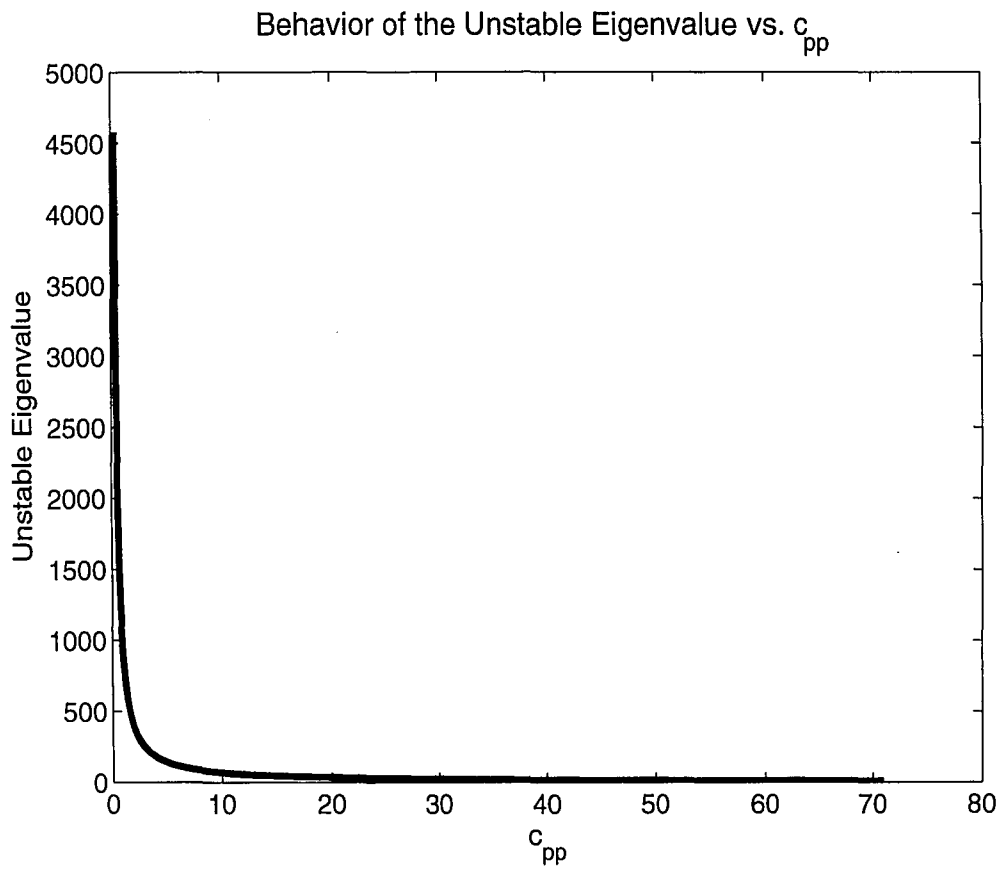$$M = \begin{bmatrix} M_{11} & M_{12} \\ M_{21} & M_{22} \end{bmatrix} \in \mathbb{C}^{(p_1+p_2)\times(q_1+q_2)},$$

Figure 2.3: Unstable Eigenvalue of the System versus c_{pp}

and letting two other complex matrices defined by $\Delta_l \in \mathbb{C}^{q_2 \times p_2}$ and $\Delta_u \in \mathbb{C}^{q_1 \times p_1}$. The *lower* LFT is defined with respect to Δ_l as the map

$$F_l(M, \bullet) : \mathbb{C}^{q_2 \times p_2} \mapsto \mathbb{C}^{p_1 \times q_1}$$

where

$$F_l(M, \Delta_l) \triangleq M_{11} + M_{12}\Delta_l(I - M_{22}\Delta_l)^{-1}M_{21}$$

assuming that $(I - M_{22}\Delta_l)^{-1}$ exists. Similarly, the *upper* LFT is defined with respect to Δ_u as the map

$$F_u(M, \bullet) : \mathbb{C}^{q_1 \times p_1} \mapsto \mathbb{C}^{p_2 \times q_2}$$

where

$$F_u(M, \Delta_u) \triangleq M_{22} + M_{21}\Delta_u(I - M_{11}\Delta_u)^{-1}M_{12}$$

assuming that $(I - M_{11}\Delta_u)^{-1}$ exists.

The matrix M is known as the *coefficient matrix*. Fig. 2.4 and Fig. 2.5 display the graphical representation of the LFT's and corresponding sets of equations.
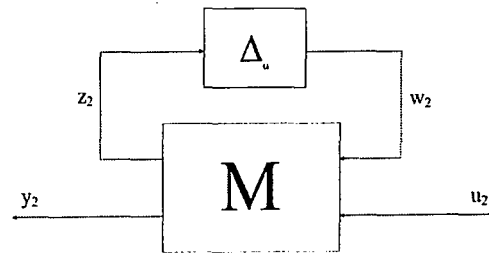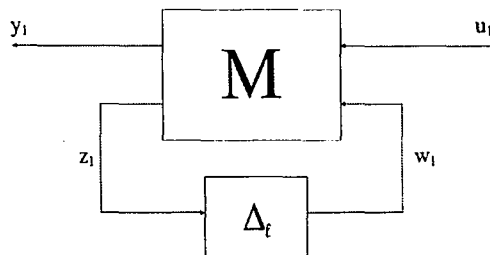

Figure 2.4: Graphical Representation of *Lower* LFT

Figure 2.5: Graphical Representation of *Upper* LFT

18

Lower LFT

$$\begin{bmatrix} y_1 \\ z_1 \end{bmatrix} = M \begin{bmatrix} u_1 \\ w_1 \end{bmatrix} = \begin{bmatrix} M_{11} & M_{12} \\ M_{21} & M_{22} \end{bmatrix} \begin{bmatrix} u_1 \\ w_1 \end{bmatrix},$$

$$w_1 = \Delta_l z_1$$

$$y_1 = F_l(M, \Delta_l) u_1$$

Upper LFT

$$\begin{bmatrix} z_2 \\ y_2 \end{bmatrix} = M \begin{bmatrix} w_2 \\ u_2 \end{bmatrix} = \begin{bmatrix} M_{11} & M_{12} \\ M_{21} & M_{22} \end{bmatrix} \begin{bmatrix} w_2 \\ u_2 \end{bmatrix},$$

$$w_2 = \Delta_u z_2$$

$$y_2 = F_u(M, \Delta_u) u_2$$

The two notations of the *upper* and *lower* LFT's are related to each other through

$$F_u(N, \Delta) = F_l(M, \Delta) \text{ where } N = \begin{bmatrix} M_{22} & M_{21} \\ M_{12} & M_{11} \end{bmatrix} \text{ [2]}.$$

2.3.2   Linear Fractional Transformation (LFT) of RWM

A system with state space representation A, B, C, D has a transfer function $G(s) = D + C(sI_n - A)^{-1}B$, where n is the number of states (or eigenvalues) in the system and I_n is the convention used to describe an $n \times n$ identity matrix. The number of states is either $n = 64$ or $n = 36$ depending on which eigenmode model is used. Defining the matrix

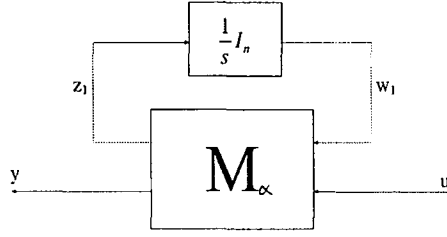$$M_\alpha = \begin{bmatrix} A & B \\ C & D \end{bmatrix}$$

19

Figure 2.6: $G(s)$ as a LFT using M_α, $\frac{1}{s}I_n$

we can write the transfer function as the linear fractional transformation of M_α as [9]

$$
\begin{aligned}
G(s) &= F_u(\begin{bmatrix} A & B \\ C & D \end{bmatrix}, \frac{1}{s}I_n) = F_u(M_\alpha, \frac{1}{s}I_n) \\
&= M_{\alpha 22} + M_{\alpha 21}\frac{1}{s}I_n(I_n - M_{\alpha 11}\frac{1}{s}I_n)^{-1}M_{\alpha 12} \\
&= D + C\frac{1}{s}I_n(I_n - A\frac{1}{s}I_n)^{-1}B = D + C(sI_n - A)^{-1}B.
\end{aligned}
$$

The graphical representation of $G(s)$ is shown in Fig. 2.6, with equivalent equations

$$
\begin{bmatrix} z_1 \\ y \end{bmatrix} = \begin{bmatrix} A & B \\ C & D \end{bmatrix}\begin{bmatrix} w_1 \\ u \end{bmatrix}
$$
$$
w_1 = \frac{1}{s}z_1
$$
$$
y = F_u(M_\alpha, \frac{1}{s}I_n)u = G(s)u.
$$

To introduce the uncertainty given by the parameterized state space system (2.9)-(2.11), the M_α matrix can be written in the form of a general affine state space uncertainty

$$
M_\alpha = \begin{bmatrix} A_0 + \sum_{i=1}^{k}\alpha_i A_i & B_0 + \sum_{i=1}^{k}\alpha_i B_i \\ C_0 + \sum_{i=1}^{k}\alpha_i C_i & D_0 + \sum_{i=1}^{k}\alpha_i D_i \end{bmatrix}
$$

where $k = 5$, $A_5 = 0, B_5 = 0$, $C_i = 0$ for $i = 1, \ldots, 4$, and $D_i = 0$ for all i.

This uncertainty can be formulated into a linear fractional transform by achieving the smallest possible repeated blocks using the method outlined in [9]. To begin this method, matrices J_i's are formed such that

$$J_i = \begin{bmatrix} A_i & B_i \\ C_i & D_i \end{bmatrix} \in \mathbb{R}^{(n+n_y) \times (n+n_u)}$$

for each $i = 1, \ldots, 5$. Then ,using singular value decomposition and grouping terms, an expression for J_i can be achieved (note: A* is denoted as the complex conjugate transpose of the matrix A)

$$\begin{aligned} J_i &= U_i \Sigma_i V_i^* = (U_i \sqrt{\Sigma_i})(\sqrt{\Sigma_i} V_i^*) \\ &= \begin{bmatrix} L_i \\ W_i \end{bmatrix} \begin{bmatrix} R_i \\ Z_i \end{bmatrix}^* . \end{aligned}$$

Denoting q_i as the rank of each matrix J_i, each inner matrix is given by

$$L_i \in \mathbb{R}^{(n \times q_i)}, W_i \in \mathbb{R}^{(n_y \times q_i)}, R_i \in \mathbb{R}^{(n \times q_i)}, Z_i \in \mathbb{R}^{(n_u \times q_i)}.$$

Then, the uncertainty can be introduced as

$$\alpha_i J_i = \begin{bmatrix} L_i \\ W_i \end{bmatrix} [\alpha_i I_{q_i}] \begin{bmatrix} R_i \\ Z_i \end{bmatrix}^* ,$$

where in our case, $q_1 = 1, q_2 = 1, q_3 = 2, q_4 = 1, q_5 = 2$. Finally, the linear fractional transformed matrix can be written as

$$M_\alpha = M_{11} + M_{12} \alpha_p M_{21},$$

where

$$M_{11} = \begin{bmatrix} A_0 & B_0 \\ C_0 & D_0 \end{bmatrix} \quad M_{12} = \begin{bmatrix} L_1 & \cdots & L_5 \\ W_1 & \cdots & W_5 \end{bmatrix}$$

$$M_{21} = \begin{bmatrix} R_1^* & Z_1^* \\ \vdots & \vdots \\ R_5^* & Z_5^* \end{bmatrix} \quad \alpha_p = \begin{bmatrix} \alpha_1 I_{q_1} & & 0 \\ & \ddots & \\ 0 & & \alpha_5 I_{q_5} \end{bmatrix}.$$

This is equivalent to the lower linear fractional transformation

$$\begin{aligned} M_\alpha &= F_l(\begin{bmatrix} M_{11} & M_{12} \\ M_{21} & 0 \end{bmatrix}, \alpha_p) = F_l(M, \alpha_p) \\ &= M_{11} + M_{12}\alpha_p(I_{q_T} - M_{22}\alpha_p)^{-1} M_{21} = M_{11} + M_{12}\alpha_p M_{21} \end{aligned}$$

where

$$M = \begin{bmatrix} M_{11} & M_{12} \\ M_{21} & 0 \end{bmatrix},$$

and q_T is the total rank of the α_p matrix given by

$$q_T = \sum_i q_i = 7.$$

Finally, the transfer function of the state space uncertainty is written as

$$G(s) = F_u(M_\alpha, \frac{1}{s}I_n) = F_u(F_l(\begin{bmatrix} M_{11} & M_{12} \\ M_{21} & 0 \end{bmatrix}, \alpha_p), \frac{1}{s}I_n).$$

The graphical representation of G(s) is shown in Fig. 2.7 with the equivalent equations

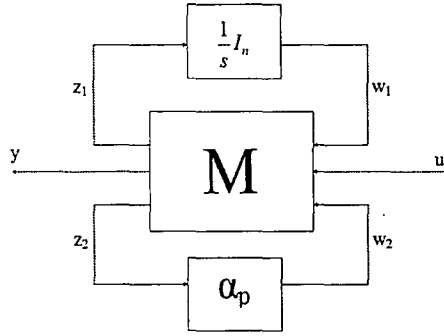Figure 2.7: G(s) as a LFT using M, α_p, $\frac{1}{s}I_n$

$$\left[\begin{array}{c} \left[\begin{array}{c} z_1 \\ y \\ z_2 \end{array}\right] \end{array}\right] = \left[\begin{array}{cc} M_{11} & M_{12} \\ M_{21} & 0 \end{array}\right] \left[\begin{array}{c} \left[\begin{array}{c} w_1 \\ u \\ w_2 \end{array}\right] \end{array}\right]$$

$$w_1 = \frac{1}{s}z_1, \quad w_2 = \alpha_p z_2$$

$$y = F_u(F_l(M, \alpha_p), \frac{1}{s}I_n)u = G(s)u.$$

2.3.3   Normalizing α Parameters

The system is now in a form where the uncertainty is given by the five α_i parameters. However, as shown earlier, each of the α_i parameters are nonlinear functions of the single variable c_{pp}. Thus the next step is to express the linear fractional transformation in terms of the single uncertainty c_{pp}. First, c_{pp} is normalized using

$$c_{pp} = d + \delta e,$$

$$d = c_{pp}^*, \quad e = max[|c_{pp_{max}} - c_{pp}^*|, |c_{pp_{min}} - c_{pp}^*|],$$

where c_{pp}^* is the nominal value of c_{pp}, and $c_{pp_{min}}$ and $c_{pp_{max}}$ are its minimum and maximum values respectively. This defines a new normalized uncertainty δ that has a range of values within $|\delta| \leq 1$ that corresponds to the desired c_{pp} range.

23

Now that each α_i parameter is expressed in terms of δ, we "pull out the δ" [10]. This is done by drawing the block diagram for each α_i system and labeling the input to each δ block z_{3_i} and the output of each δ block w_{3_i}. Then the matrix Q, which satisfies $\alpha_p = F_l(Q, \Delta)$ with $\Delta = \delta I_{m_T}$, can be found using $\begin{bmatrix} w_{2_i} \\ z_{3_i} \end{bmatrix} \triangleq Q_i \begin{bmatrix} z_{2_i} \\ w_{3_i} \end{bmatrix}$ for each α_i term, where m_T is the total number of uncertainty elements needed to represent α_p. Thus the Q_i matrix satisfies the equation $\alpha_i = F_l(Q_i, \delta I_{m_i})$, where m_i is the minimum number of uncertainty elements δ needed to represent α_i. Recalling that $w_2 = \alpha_p z_2$, the system can be formulated such that $w_2 = F_l(Q, \Delta) z_2$. To correspond to each α_i term in the matrix α_p, the w_2, z_2, w_3, z_3 matrices are given by

$$w_2 = \begin{bmatrix} w_{2_1} \\ w_{2_2} \\ w_{2_3} \\ w_{2_4} \\ w_{2_5} \end{bmatrix}, z_2 = \begin{bmatrix} z_{2_1} \\ z_{2_2} \\ z_{2_3} \\ z_{2_4} \\ z_{2_5} \end{bmatrix}, w_3 = \begin{bmatrix} z_{3_1} \\ z_{3_2} \\ z_{3_3} \\ z_{3_4} \\ z_{3_5} \end{bmatrix}, z_3 = \begin{bmatrix} z_{3_1} \\ z_{3_2} \\ z_{3_3} \\ z_{3_4} \\ z_{3_5} \end{bmatrix},$$

where each w_{2_i} and z_{2_i} are vectors of length q_i, based on the rank of each J_i matrix, and each w_{3_i} and z_{3_i} are vectors of length $m_i q_i$, based on the minimum number of δ's required to represent each α_i and the value of q_i. The composite Q matrix will be defined after each individual Q_i is determined, where Q_i is given by $Q_i = \begin{bmatrix} Q_{i_{11}} & Q_{i_{12}} \\ Q_{i_{21}} & Q_{i_{22}} \end{bmatrix}$. The total number of uncertainty elements m_T for α_p is given by the total length of w_3, which is found by

$$m_T = \sum_i m_i q_i.$$

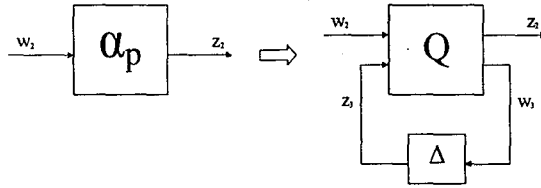The graphical representation of the α_p block is show in Fig. 2.8.

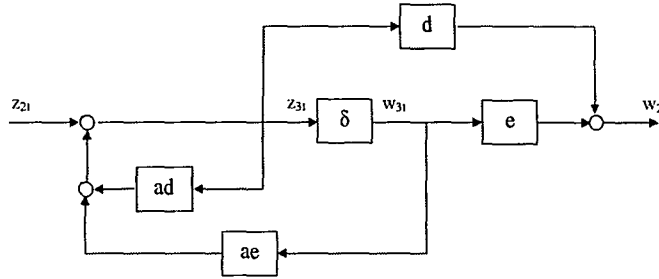Figure 2.8: α_p as a LFT using Q and Δ

Figure 2.9: Block Diagram for α_1

The block diagram for α_1 is shown in Fig. 2.9. Recalling that $\alpha_1 = \frac{c_{pp}}{1-c_{pp}u_1'M_{ss}^{-1}u_1}$, and using $a = u_1'M_{ss}^{-1}u_1$, the relationship becomes

$$\alpha_1 = \frac{c_{pp}}{1 - ac_{pp}}.$$

Inserting the normalized relationship $c_{pp} = d + \delta e$, α_1 can be written as

$$\alpha_1 = \frac{d + \delta e}{1 - a(d + \delta e)} = \frac{d + \delta e}{(1 - ad) - ae\delta}.$$

Since there is only one uncertainty element, $m_1 = 1$. The block diagram for α_1 can be directly drawn from this form, with the feedback terms in the denominator and the feedforward terms in the numerator. The terms not multiplied by δ are branched out prior to the δ block and those multiplied by δ are branched out after the δ block. The terms in the denominator are multiplied by -1 because of the feedback (Fig. 2.9). From the diagram,

$$z_{3_1} = z_{2_1} + \left(adz_{3_1} + aew_{3_1} \right).$$

25

Solving for z_{3_1}

$$z_{3_1} - adz_{3_1} = z_{2_1} + aew_{3_1}$$

$$z_{3_1}(1 - ad) = z_{2_1} + aew_{3_1}$$

$$z_{3_1} = \left(\frac{1}{1 - ad}\right)z_{2_1} + \left(\frac{ae}{1 - ad}\right)w_{3_1}.$$

From the diagram, the output is given by

$$w_{2_1} = dz_{3_1} + ew_{3_1}.$$

Substituting for z_{3_1}, the expression becomes

$$w_{2_1} = d\left[\left(\frac{1}{1 - ad}\right)z_{2_1} + \left(\frac{ae}{1 - ad}\right)w_{3_1}\right] + ew_{3_1}$$

$$= \left(\frac{d}{1 - ad}\right)z_{2_1} + \left(\left[\frac{aed}{1 - ad}\right] + e\right)w_{3_1}$$

$$= \left(\frac{d}{1 - ad}\right)z_{2_1} + \left(e\left[1 + \frac{ad}{1 - ad}\right]\right)w_{3_1}.$$

Thus, the governing equation for α_1 is given by

$$\begin{bmatrix} w_{2_1} \\ z_{3_1} \end{bmatrix} = Q_1 \begin{bmatrix} z_{2_1} \\ w_{3_1} \end{bmatrix},$$

which results in a Q_1 given by

$$Q_1 = \begin{bmatrix} \frac{d}{1-ad} & e\left[1 + \frac{ad}{1-ad}\right] \\ \frac{1}{1-ad} & \frac{ae}{1-ad} \end{bmatrix} = \begin{bmatrix} Q_{1_{11}} & Q_{1_{12}} \\ Q_{1_{21}} & Q_{1_{22}} \end{bmatrix}.$$

To prove that this is equivalent to $\alpha_1 = F_l(Q_1, \delta)$, the lower linear fractional tranform

is expanded

$$
\begin{aligned}
\alpha_1 &= F_l\left(Q_1, \delta\right) = Q_{1_{11}} + Q_{1_{12}}\delta\left(1 - Q_{1_{22}}\delta\right)^{-1} Q_{1_{21}} \\
&= \left(\frac{d}{1-ad}\right) + \left(e\left[1 + \frac{ad}{1-ad}\right]\right)\delta\left(1 - \left(\frac{ae}{1-ad}\right)\right)^{-1}\left(\frac{1}{1-ad}\right) \\
&= \frac{d}{1-ad} + e\left(\frac{1}{1-ad}\right)\delta\left(\frac{1-ad-ae\delta}{1-ad}\right)^{-1}\frac{1}{1-ad} \\
&= \frac{d}{1-ad} + \frac{e\delta}{\left(1-ad\right)\left(1-ad-ae\delta\right)} \\
&= \frac{d\left(1-ad\right) - aed\delta + e\delta}{\left(1-ad\right)\left(1-ad-ae\delta\right)} \\
&= \frac{d\left(1-ad\right) + e\delta\left(1-ad\right)}{\left(1-ad\right)\left(1-ad-ae\delta\right)} \\
&= \frac{d+\delta e}{\left(1-ad\right) - ae\delta}.
\end{aligned}
$$

For the system matrices of the DIII-D tokamak, the behavior of α_1 and α_2 are approximately the same, with an error on the order of 10^{-12}. From this very good approximation, we can take $\alpha_1 = \alpha_2$. Although the full model could be used, this is an accurate enough assumption that allows the reduction of computational complexity. As a result of this approximation, the following changes can be made to the other α parameters:

$$
\alpha_3 = \alpha_2\alpha_1 \qquad \Rightarrow \qquad \alpha_3 = \alpha_1^2
$$

$$
\alpha_4 = \alpha_2\alpha_1^2 \qquad \Rightarrow \qquad \alpha_4 = \alpha_1^3.
$$

Since $\alpha_2 = \alpha_1$, $m_2 = m_1 = 1$ and the Q_2 block is simply defined by

$$
Q_2 = Q_1.
$$

The parameter α_3 is given as $\alpha_3 = \alpha_1^2$, or $\alpha_3 = F_l(Q_1, \delta) \cdot F_l(Q_1, \delta)$. In general,

the series connection of x identical lower linear fractional transforms $F_l(T, \delta)$ where

$$T = \begin{bmatrix} T_{11} & T_{12} \\ T_{21} & T_{22} \end{bmatrix}$$

can be written as $F_l(S, \delta I_x)$, where

$$S = \begin{bmatrix} T_{11}^x & T_{11}^{x-1}T_{12} & T_{11}^{x-2}T_{12} & \cdots & T_{11}T_{12} & T_{12} \\ \hline T_{21} & T_{22} & & \cdots & & 0 \\ T_{21}T_{11} & T_{21}T_{12} & T_{22} & & & \\ \vdots & \vdots & T_{21}T_{12} & T_{22} & & \vdots \\ T_{21}T_{11}^{x-2} & T_{21}T_{11}^{x-3}T_{12} & \cdots & T_{21}T_{12} & T_{22} & \\ T_{21}T_{11}^{x-1} & T_{21}T_{11}^{x-2}T_{12} & T_{21}T_{11}^{x-3}T_{12} & \cdots & T_{21}T_{12} & T_{22} \end{bmatrix}.$$

A reduction can be made so that $\alpha_3 = F_l(Q_3, \delta I_2)$, where I_2 is the size 2 identity matrix, thus $m_3 = 2$. Through the series connection of the linear fractional transform of Q_1, the Q_3 block is given by

$$Q_3 = \begin{bmatrix} Q_{1_{11}}^2 & Q_{1_{11}}Q_{1_{12}} & Q_{1_{12}} \\ \hline Q_{1_{21}} & Q_{1_{22}} & 0 \\ Q_{1_{21}}Q_{1_{11}} & Q_{1_{21}}Q_{1_{12}} & Q_{1_{22}} \end{bmatrix}.$$

Similarly to Q_3, the parameter α_4 is given as $\alpha_4 = \alpha_1^3$, or $\alpha_4 = F_l(Q_1, \delta) \cdot F_l(Q_1, \delta) \cdot F_l(Q_1, \delta)$. A reduction can be made so that $\alpha_4 = F_l(Q_4, \delta I_3)$, where I_3 is the size 3 identity matrix, $m_4 = 3$, and Q_4 is given by the series connection of the linear
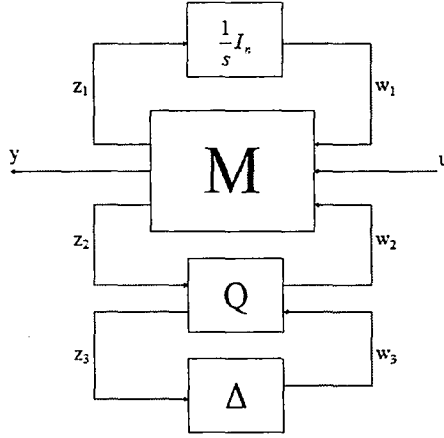
Figure 2.10: G(s) as a LFT using M, Q, δ, $\frac{1}{s}I_n$

fractional transform such that

$$
Q_4 = \left[\begin{array}{c|ccc}
Q^3_{1_{11}} & Q^2_{1_{11}}Q_{1_{12}} & Q_{1_{11}}Q_{1_{12}} & Q_{1_{12}} \\
\hline
Q_{1_{21}} & Q_{1_{22}} & 0 & 0 \\
Q_{1_{21}}Q_{1_{11}} & Q_{1_{21}}Q_{1_{12}} & Q_{1_{22}} & 0 \\
Q_{1_{21}}Q^2_{1_{11}} & Q_{1_{21}}Q_{1_{11}}Q_{1_{12}} & Q_{1_{21}}Q_{1_{12}} & Q_{1_{22}}
\end{array} \right] .
$$

Also, Q_5 can be directly written as

$$
Q_5 = \left[\begin{array}{cc}
d & e \\
1 & 0
\end{array} \right] ,
$$

such that $m_5 = 1$.

Now that there is an expression for each of the α_i $(i = 1, \ldots, 5)$ parameters in terms of a linear fractional transformation $\alpha_i = F_l(Q_i, \delta I_{m_i})$, they can be combined to form one linear fraction transformation with a common uncertainty δ. As shown

29
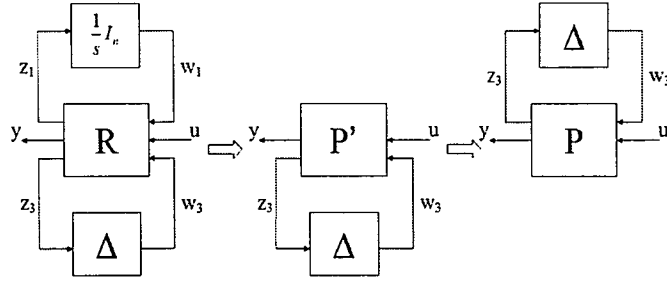
Figure 2.11: Graphical representation of $G(s)$ manipulation

earlier, the uncertainty in terms of α is given as

$$
\alpha_p = \begin{bmatrix} \alpha_1 I_{q_1} & & & & 0 \\ & \alpha_2 I_{q_2} & & & \\ & & \alpha_3 I_{q_3} & & \\ & & & \alpha_4 I_{q_4} & \\ 0 & & & & \alpha_5 I_{q_5} \end{bmatrix},
$$

where I_{q_i} is the size q_i identity matrix. The total number of uncertain elements is given by $m_T = \sum_i m_i q_i = 11$. Thus, the linear fractional transformation $\alpha_p = F_l(Q, \Delta)$ with $\Delta = \delta I_{m_T}$ is given by $\alpha_p = Q_{11} + Q_{12}\Delta(I_{m_T} - Q_{22}\Delta)^{-1}Q_{21}$ where $Q = \begin{bmatrix} Q_{11} & Q_{12} \\ Q_{21} & Q_{22} \end{bmatrix}$. Each submatrix Q_{jk} is given by the block diagonal matrix

$$
Q_{jk} = \begin{bmatrix} Q_{1_{jk}} & & 0 \\ & \ddots & \\ 0 & & Q_{5_{jk}} \end{bmatrix}
$$

where $j = 1, 2$ and $k = 1, 2$. The matrix Q_{jk} has the same number of diagonal blocks as α_p based on the rank of each J_i matrix denoted by q_i.

This renders the final representation of entire system $G(s) = F_u(F_l(M, F_l(Q, \Delta)), \frac{1}{s}I_n)$, which is described by Fig. 2.10 and corresponding equation set

30

$$\left[\begin{bmatrix} z_1 \\ y \\ z_2 \end{bmatrix}\right] = \begin{bmatrix} M_{11} & M_{12} \\ M_{21} & 0 \end{bmatrix} \left[\begin{bmatrix} w_1 \\ u \\ w_2 \end{bmatrix}\right]$$

$$\begin{bmatrix} w_2 \\ z_3 \end{bmatrix} = \begin{bmatrix} Q_{11} & Q_{12} \\ Q_{21} & Q_{22} \end{bmatrix} \begin{bmatrix} z_2 \\ w_3 \end{bmatrix}$$

$$w_1 = \frac{1}{s}z_1, \quad w_3 = \delta z_3$$

$$y = F_u(F_l(M, F_l(Q, \Delta)), \frac{1}{s}I_n)u = G(s)u.$$

Finally, the original system M can be combined with the matrix Q through the interconnection of LFT's [11]. This is done using the fact that

$$M_\alpha = F_l(M, \alpha_p) = F_l(M, F_l(Q, \Delta)) = F_l(R, \Delta) = F_l(R, \Delta)$$

where R is defined as

$$R \triangleq \begin{bmatrix} R_{11} & R_{12} \\ R_{21} & R_{22} \end{bmatrix},$$

and where

$$R_{11} = M_{11} + M_{12}Q_{11}(I_1 - M_{22}Q_{11})^{-1}M_{21}$$

$$R_{12} = M_{12}(I_1 - Q_{11}M_{22})^{-1}Q_{12}$$

$$R_{21} = Q_{21}(I_1 - M_{22}Q_{11})^{-1}M_{21}$$

$$R_{22} = Q_{22} + Q_{21}M_{22}(I_1 - Q_{11}M_{22})^{-1}Q_{12}$$

Since $M_{22} = 0$ it simplifies to

$$R = \begin{bmatrix} M_{11} + M_{12}Q_{11}M_{21} & M_{12}Q_{12} \\ Q_{21}M_{21} & Q_{22} \end{bmatrix}.$$

Now the system is reduced to a simple form of R, uncertainty $\Delta = \delta I_{m_T}$ with $|\delta| \leq 1$, and $\frac{1}{s}I_n$. The system can now be reduced using a simple property of the LFT. The system given by $G(s) = F_u(F_l(R, \Delta), \frac{1}{s}I_n)$ can be written as $G(s) = F_l(F_u(R, \frac{1}{s}I_n), \Delta) = F_l(P', \Delta)$ where $P' = F_u(R, \frac{1}{s}I_n)$. The final step in the system reduction moves the uncertainty, creating an upper LFT for convention purposes. This is done by using

$$G(s) = F_l(P', \Delta) = F_u(P, \Delta)$$

where P' is of the form

$$P' = \begin{bmatrix} P'_{11} & P'_{12} \\ P'_{21} & P'_{22} \end{bmatrix} \quad and \quad P = \begin{bmatrix} P'_{22} & P'_{21} \\ P'_{12} & P'_{11} \end{bmatrix}.$$

The overall system reduction is shown in Fig. 2.11.

The parameterization of the RWM model allows this system to be represented in the general framework of robust control for uncertain systems. The goal is to design a controller K that stabilizes the plant for all uncertainty $|\delta| \leq 1$. The feedback controller K can be applied to the plant to formulate a closed-loop LFT system on the uncertainty and the controller, given by

$$\begin{aligned} G(s) &= F_l(F_u(P, \Delta), K) \\ &= F_u(F_l(P, K), \Delta), \end{aligned}$$
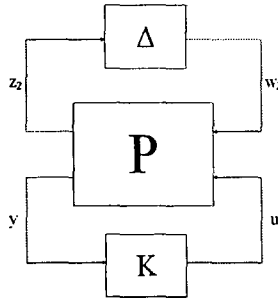
which can be seen in Fig. 2.12.

Figure 2.12: General framework for robust control

2.4 Model Characteristics

The model matrices are provided by FAR-TECH Inc. using experimental data to determine the values. As mentioned in the introduction, the model uses a typical quartet structure of 240 degrees. This configuration takes the 12 control I-coils (6 pairs) and locks the amplitude and phase relationship between several of the I-coils, leaving 3 I-coils that can be used for control purposes. The 3 C-coils have a much slower response, have little to no effect on the rapid RWM instability, and are not considered as control inputs. Thus, the number of controllable inputs into the model can be taken as 3, corresponding to the 3 I-coils. And using the matched filter, the number of outputs is reduced from the 23 sensors to the 2 components of the RWM mode. The frequency response graphs for the model in Fig. 2.13-Fig. 2.15 clearly display the effect of the uncertainty on the system. As seen by the majority of the frequency response figures, the uncertainty strongly effects the phase and magnitude of the lower frequencies compared to that of higher frequencies. Also seen by these figures, at varying uncertainty values the frequency response takes a similar profile except for high growth rates γ (small values of c_{pp}), which introduced more error from the nominal system.

The frequency response graphs were produced using both the original model matrices and the model in $P\Delta$ form to ensure the validity of the transformation (Fig. 2.16-Fig. 2.18). To easily make the comparison, the frequency response graphs are com-

puted at three growth rates, the minimum, nominal, and maximum values of the range we are considering. The values are $\gamma = 10 rad/s$, $\gamma = 120 rad/s$, and $\gamma = 5,000 rad/s$ ($c_{pp} = 71$, $c_{pp} = 5.75$, and $c_{pp} = 0.3325$). All of the input to output combinations match well between the two systems, with small error introduced in the Input 3 to Output 1 case in Fig. 2.18. This error is negligible for the controller design.

2.5 Discrete-Time Transformation of the State Matrices

The model transformation into the nominal plant/uncertainty form benefits the application of μ-synthesis to obtain one controller that can provide robust stability. However, this transformation can also lead to the design of another controller technique, adaptive control via system identification. The purpose of the adaptive control approach is to use the knowledge of the model to perform online estimation of the growth rate γ, from which an optimal controller for that growth rate can be applied. Before an adaptive controller can be designed, real time parameter estimation must be obtained through system identification techniques. Since all of the recursive parameter estimation methods (RPEM) involve using a discrete-time state equation, the first step is to make a discrete-time equivalent state equation. Sampling of the system $\dot{x} = Ax + Bu$ will produce a discrete-time system

$$x_{k+1} = Fx_k + Gu_k,$$

where $F = e^{AT}$, $G = \int_0^T e^{A\tau} B d\tau$, and T is the sampling time. These matrices cannot be implemented in this form because of the exponential function, therefore an approximation of the exponential function is needed. The exponential can be written
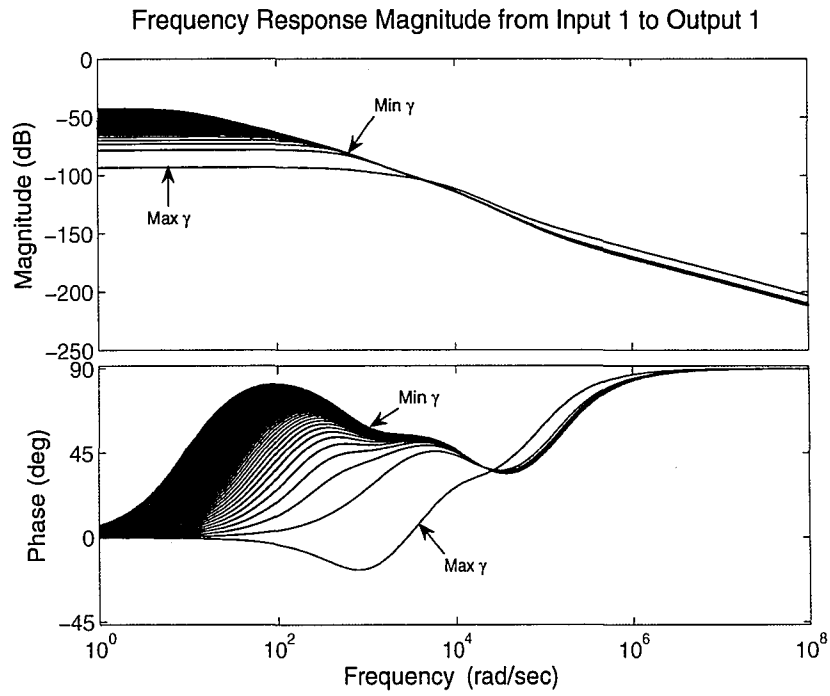
34
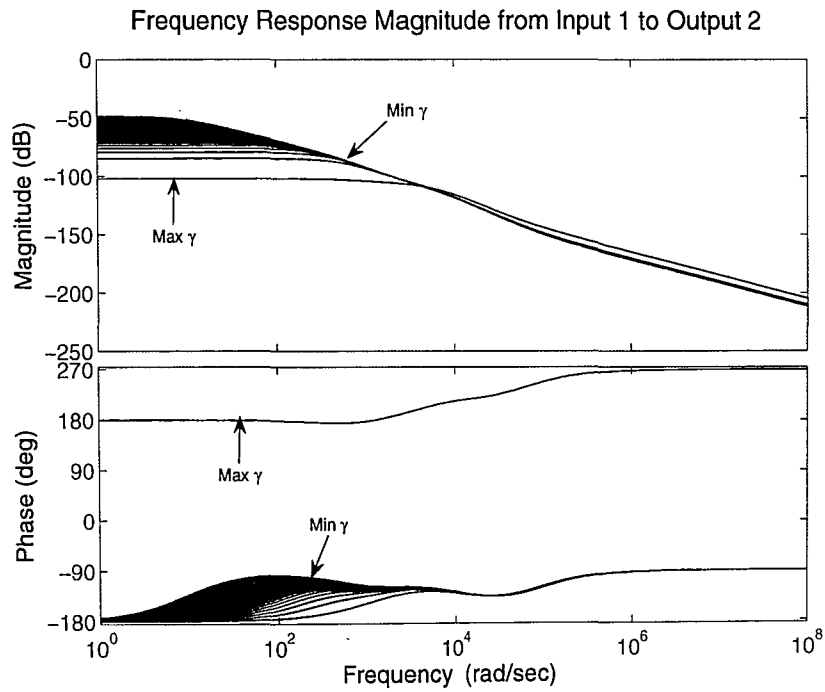
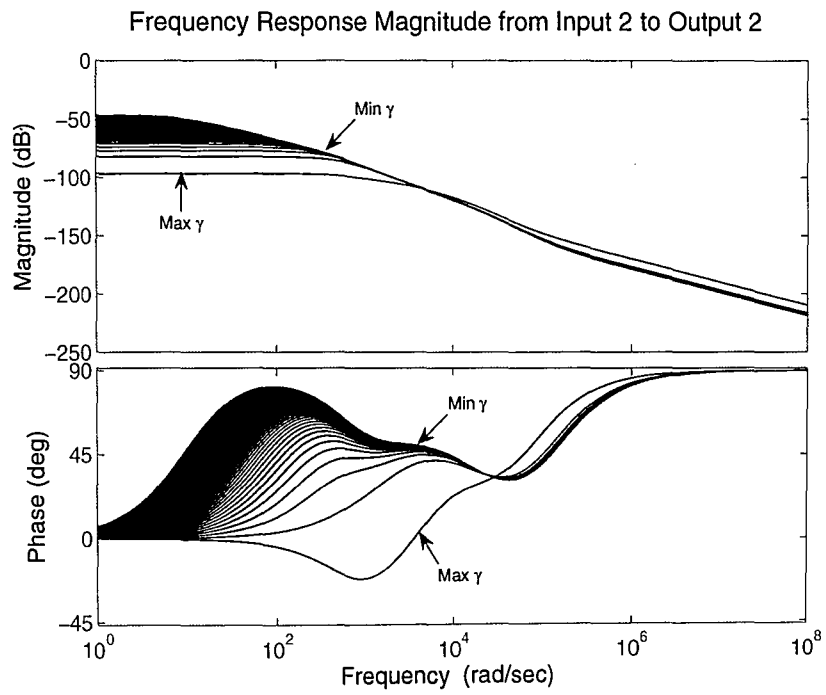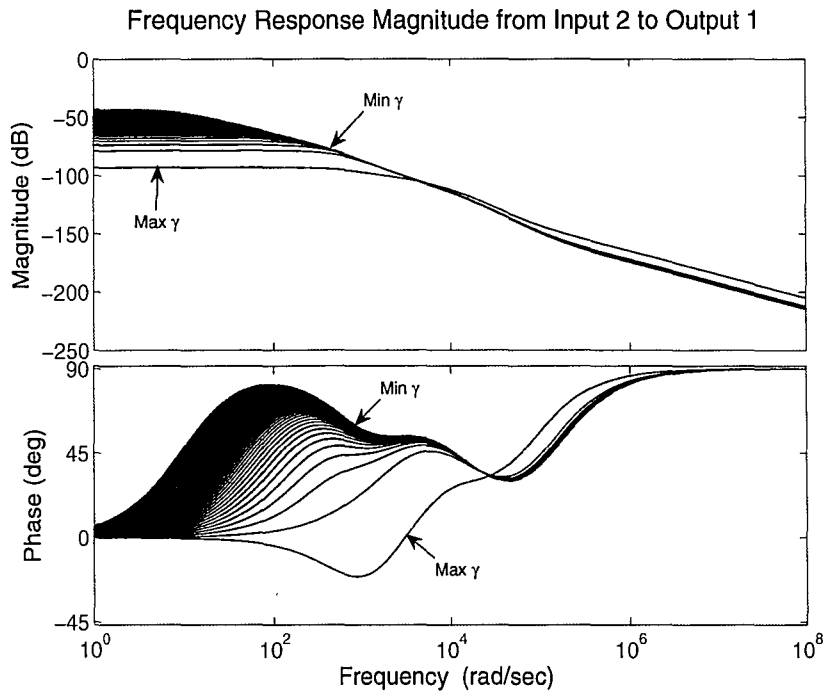Figure 2.13: Frequency Response from Input 1 to (a) Output 1 and (b) Output 2

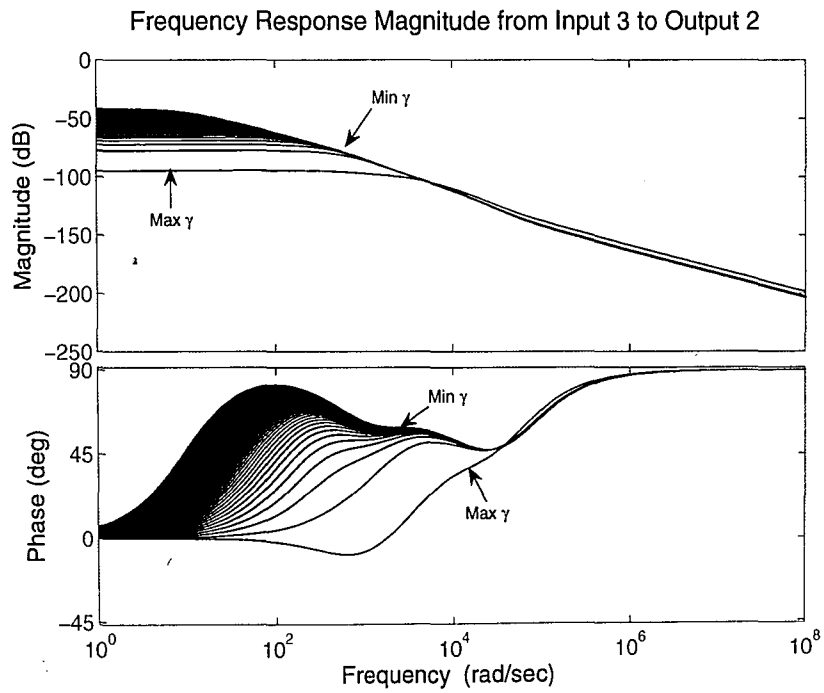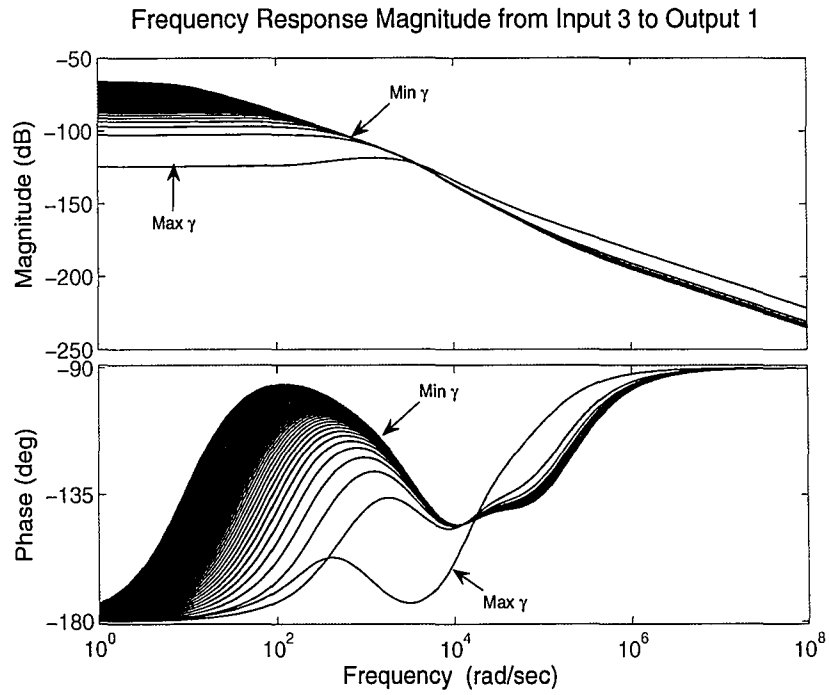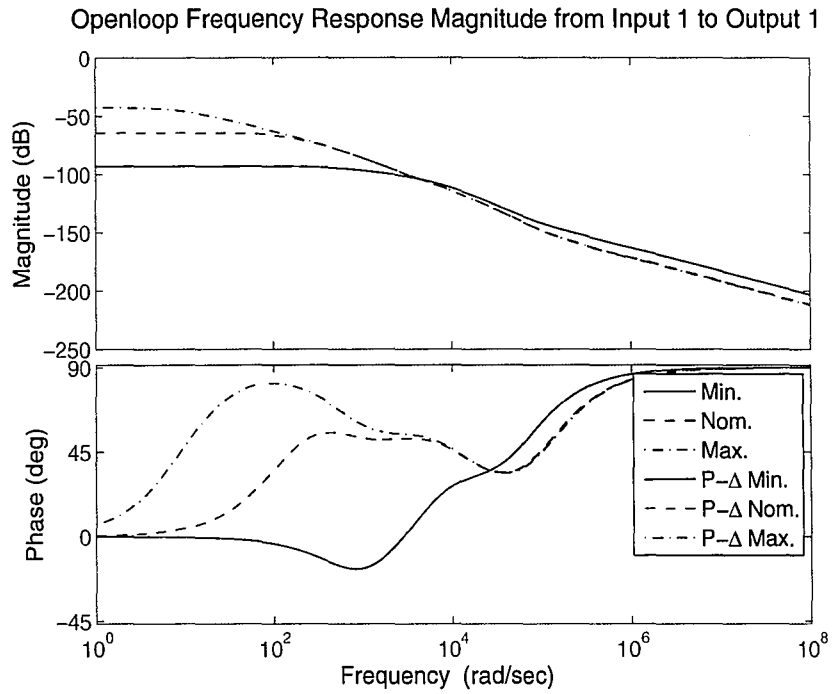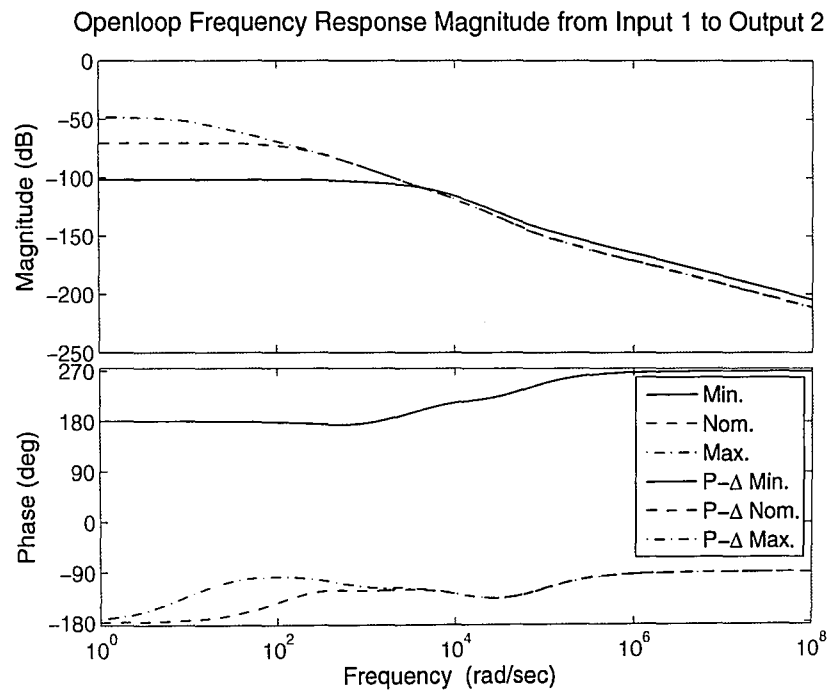Figure 2.14: Frequency Response from Input 2 to (a) Output 1 and (b) Output 2

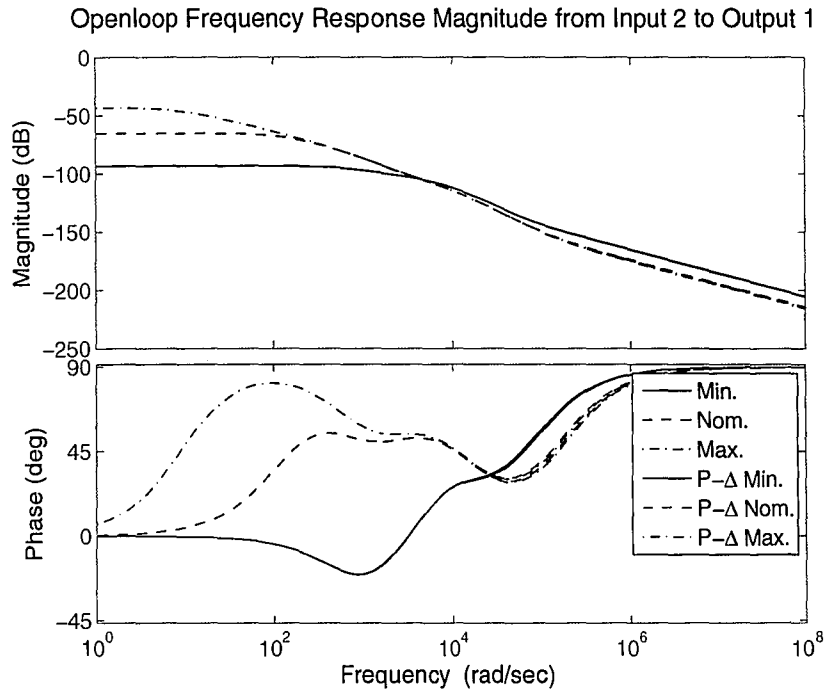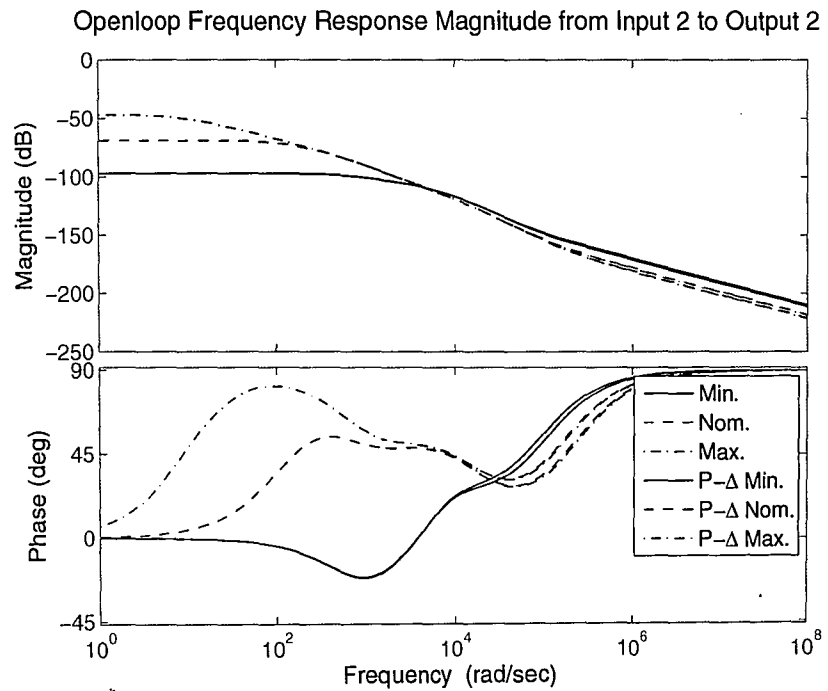Figure 2.15: Frequency Response from Input 3 to (a) Output 1 and (b) Output 2

Openloop Frequency Response Magnitude from Input 1 to Output 1

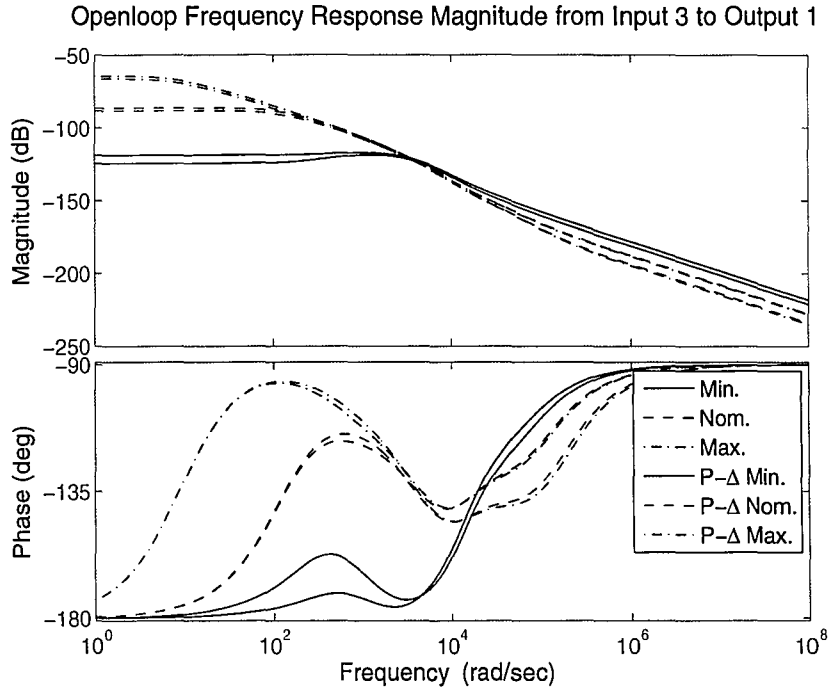(a)

Openloop Frequency Response Magnitude from Input 1 to Output 2

(b)

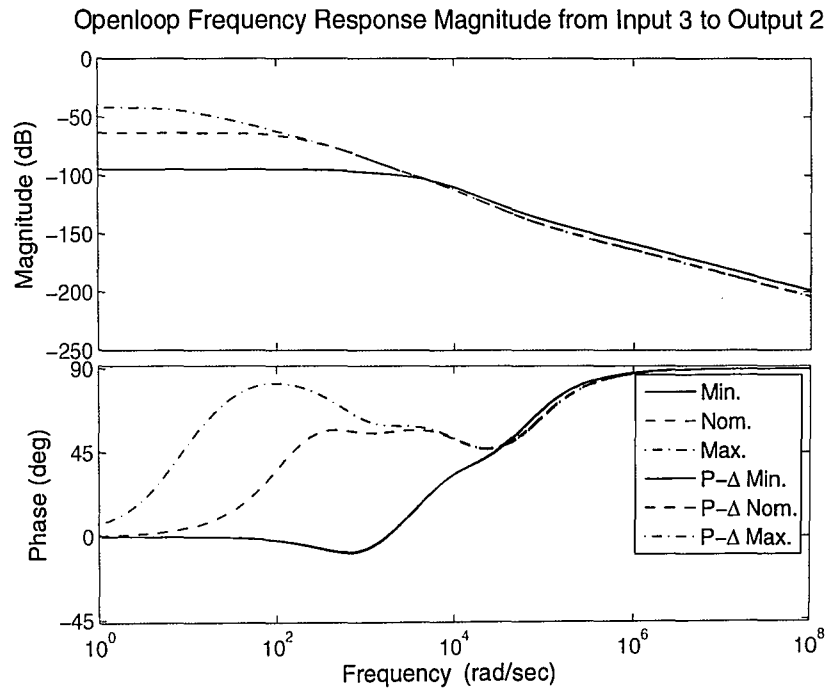Figure 2.16: Frequency Response Comparison from Input 1 to (a) Output 1 and (b) Output 2

Figure 2.17: Frequency Response Comparison from Input 2 to (a) Output 1 and (b) Output 2

Figure 2.18: Frequency Response Comparison from Input 3 to (a) Output 1 and (b) Output 2

as

$$e^{AT} = I + AT + A^2\frac{T^2}{2!} + A^3\frac{T^3}{3!} + ... = I + \sum_{k=1}^{\infty} \frac{A^k T^k}{k!}.$$

In order to approximate the state matrices, the number of terms in the exponential function expansion must be determined. A common method of determining how many terms to keep is Paynter's algorithm which follows the steps:

1. Let $q = max|A_{ij}T|$ where A is $n \times n$

2. Find an integer p such that $\frac{1}{p}(nq)^p e^{nq} \approx 0.001$

3. Compute $\Psi = I + \frac{1}{2!}AT + \frac{1}{3!}A^2T^2 + ... + \frac{1}{(p+1)!}A^pT^p$, truncating the series after p terms

4. Form $F = I + AT\Psi$, $G = \Psi TB$.

This algorithm is implemented in the Matlab code to obtain the discrete-time state matrices. Also needed for the parameter estimation algorithm are the derivatives of these state matrices with respect to the parameter c_{pp}. First, rewriting the discrete-time matrices

$$F = I + AT\Psi = I + AT\left(I + \sum_{k=1}^{p} \frac{A^k T^k}{(k+1)!} \right) = I + \sum_{k=1}^{p+1} \frac{A^k T^k}{k!}$$

$$G = \Psi TB.$$

Now the derivatives can be expressed as

$$\frac{dF}{dc_{pp}} = \left[\sum_{k=1}^{p+1} \frac{kA^{k-1}T^k}{k!} \right] \frac{dA}{dc_{pp}}$$

$$\frac{dG}{dc_{pp}} = \frac{d\Psi}{dc_{pp}}TB + \Psi T\frac{dB}{dc_{pp}},$$

where

$$\frac{d\Psi}{dc_{pp}} = \left[\sum_{k=1}^{p} \frac{kA^{k-1}T^k}{(k+1)!} \right] \frac{dA}{dc_{pp}}.$$

The derivatives of the continuous-time state matrices can be found using the form

$A = \sum_{j=0}^{4} \alpha_j A_j$ and $B = \sum_{j=0}^{4} \alpha_j B_j$, where the A_j and B_j matrices are constant and only the α_j terms depend on c_{pp}. Thus the derivatives with respect to c_{pp} can be written as

$$\frac{dA}{dc_{pp}} = \sum_{j=0}^{4} \frac{d\alpha_j}{dc_{pp}} A_j$$

$$\frac{dB}{dc_{pp}} = \sum_{j=0}^{4} \frac{d\alpha_j}{dc_{pp}} B_j.$$

Knowing that the α terms are given by

$$\alpha_0 = 1$$

$$\alpha_1 = \frac{c_{pp}}{1 - c_{pp} v_1' M_{ss}^{-1} u_1}$$

$$\alpha_2 = \frac{c_{pp}}{1 - c_{pp} v_2' M_{ss}^{-1} u_2 - \frac{c_{pp}^2}{1 - c_{pp} v_1' M_{ss}^{-1} u_1} v_2'(M_{ss}^{-1} u_1)(v_1' M_{ss}^{-1}) u_2}$$

$$\alpha_3 = \alpha_2 \alpha_1$$

$$\alpha_4 = \alpha_2 \alpha_1^2$$

the derivatives are given as

$$\frac{\alpha_0}{dc_{pp}} = 0$$

$$\frac{\alpha_1}{dc_{pp}} = \frac{1}{\left(1 - c_{pp} v_1' M_{ss}^{-1} u_1\right)^2}$$

$$\frac{\alpha_2}{dc_{pp}} = \frac{\left(1 - c_{pp} v_1' M_{ss}^{-1} u_1\right)^2 + c_{pp}^2 \left(v_2' M_{ss}^{-1} u_1 v_1' M_{ss}^{-1} u_2\right)}{\left(\begin{array}{l} 1 - c_{pp} v_1' M_{ss}^{-1} u_1 - c_{pp} v_2' M_{ss}^{-1} u_2 + c_{pp}^2 \left(v_2' M_{ss}^{-1} u_2 v_1' M_{ss}^{-1} u_1\right) \\ \qquad\qquad\qquad\qquad -c_{pp}^2 \left(v_2' M_{ss}^{-1} u_1 v_1' M_{ss}^{-1} u_2\right) \end{array} \right)^2}$$

$$\frac{\alpha_3}{dc_{pp}} = \frac{d\alpha_2}{dc_{pp}} \alpha_1 + \alpha_2 \frac{d\alpha_1}{dc_{pp}}$$

$$\frac{\alpha_4}{dc_{pp}} = \frac{d\alpha_2}{dc_{pp}} \alpha_1^2 + 2\alpha_2 \alpha_1 \frac{d\alpha_1}{dc_{pp}}.$$

A comparison check was run on the discrete-time system versus the continuous-

time system. The comparison can be seen in Fig. 2.19. The left column is the continuous system, and the right column is the discrete system. All three graphs match well for the discretization. All the simulations were run at $c_{pp} = 5.75$.
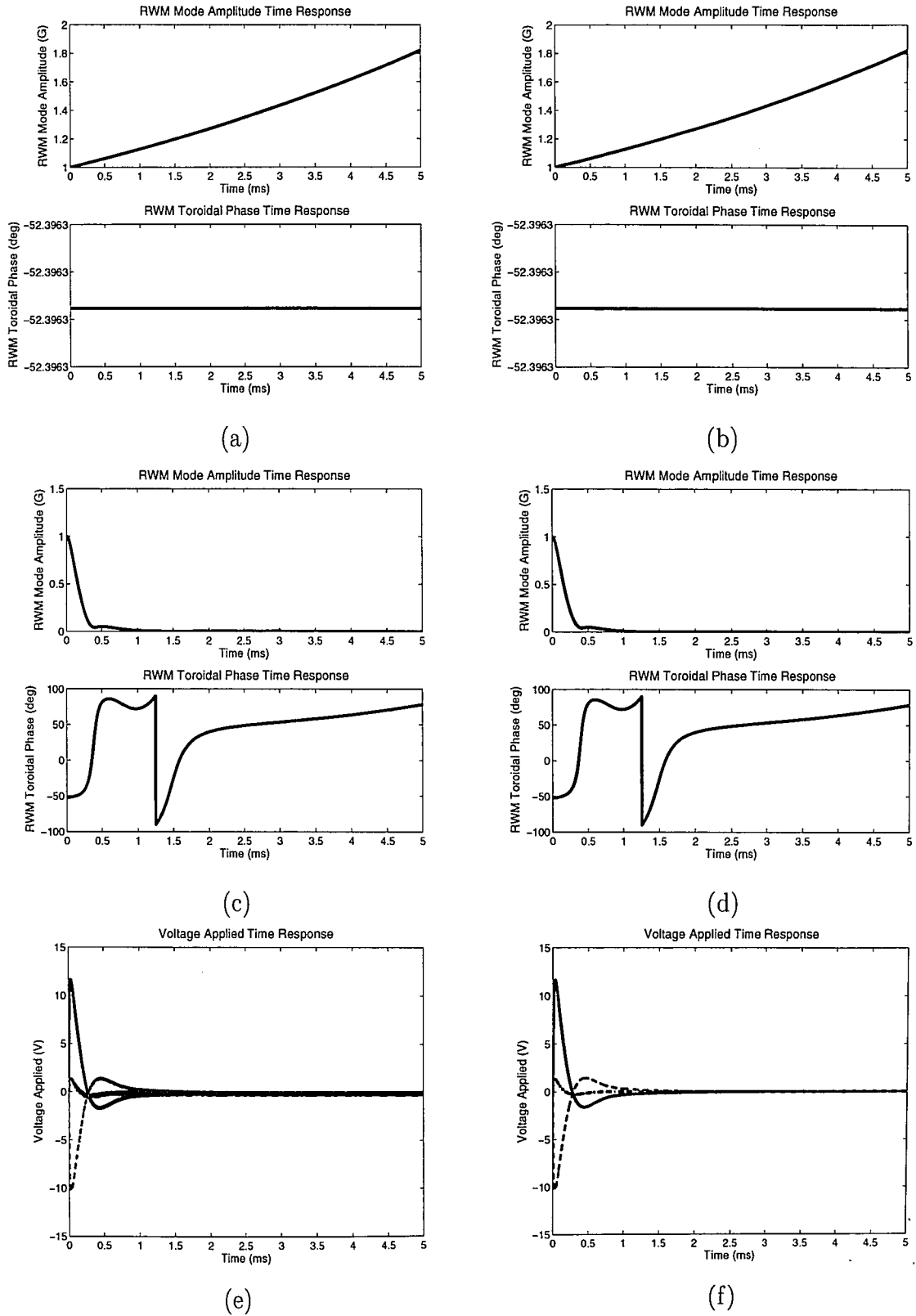
Figure 2.19: Comparison for (a)-(b) Output of open-loop simulation, (c)-(d) Output of closed-loop simulation, and (e)-(f) Controller of closed-loop simulation.

44

Chapter 3

Controller Design

Although the main focus was to design a robust controller for the RWM model, in order to have an effective comparison of controllers other controller design schemes were considered. The controller designs used were DK, NCF, PD, $LQRY$, and LQG.

3.1 DK-iteration Model Based Controller

The goal is to design a controller that can robustly stabilize the RWM and meet specified controller performance criteria. That is equivalent to designing a feedback controller K that robustly stabilizes the system for the applicable range of Δ in Fig. 2.12. The basic idea is that for a small enough disturbance in the uncertain parameter, stability can be maintained. Thus, μ-analysis gives a non-conservative measure of the range in which this disturbance exists and the system remains stable. The robust stability of the plant is determined by the N_{11} sub-matrix, where $N = F_l(P, K)$. P is the system that relates the control input, the sensor output, and the growth rate of the RWM through the reformulation of the plasma model (Fig. 2.12). The system N represents the nominal closed-loop system. The sub-system N_{11} term isolates the uncertainty from the input and output of the system. Meanwhile, N_{12}

and N_{21} characterize the coupling between the uncertainty and the input/output of the system and N_{22} represents the system at a nominal c_{pp} value ($\Delta = 0$). The robust stability is determined by the structured singular value, which is defined as

$$\mu(N_{11}) \triangleq \frac{1}{min\{k_m | det(I - k_m N_{11}\Delta) = 0\}}$$

for $\bar{\sigma}(\Delta) \leq 1$. Lager μ values means $(I - N_{11}\Delta)$ becomes singular with small perturbations, thus the smaller μ the better. The robust stability condition is found by finding the smallest value of k_m at the onset of instability, or $det(I - k_m N_{11}\Delta) = 0$, which yields $k_m = \frac{1}{\mu(N_{11})}$, where k_m is a measure of the robust stability to perturbations in Δ. Thus, assuming N_{11} and Δ are stable, the system is robustly stable if and only if $\mu(N_{11}(j\omega)) < 1, \forall \omega$. Similarly, the robust performance is given by $\mu(N) < 1, \forall \omega$. Both conditions assume that N is internally stable. For this application of the μ-synthesis controller, there is no weight augmented to the system to affect the performance of the design.

DK-iteration is one available procedure to design a controller using μ-synthesis. Since there is no direct method to synthesize a μ-optimal controller, this method is used by combining $\mathcal{H}_\infty$ synthesis and μ-analysis. This method starts with the upper bound on μ in terms of the scaled singular value

$$\mu(N) \leq \min_{D \in \mathcal{D}} \bar{\sigma}\left(DND^{-1}\right)$$

where $\mathcal{D}$ is the set of matrices D which commute with Δ, i.e., $D\Delta = \Delta D$. Then, the controller that minimizes the peak value over frequency of this upper bound is found, namely

$$\min_K \left(\min_{D \in \mathcal{D}} \|DN(K)D^{-1}\|_\infty\right).$$

The controller is designed by alternating between the two minimization problems until reasonable performance is achieved. The DK-iteration steps are summarized in

[11] as follows:

1. K-step. Synthesize an $\mathcal{H}_\infty$ controller for the scaled problem, $\min_K |DN(K)D^{-1}|_\infty$ with fixed D(s).

2. D-step. Find D($j\omega$) to minimize $\bar{\sigma}\left(DND^{-1}(j\omega)\right)$ at each frequency with fixed N.

3. Fit the magnitude of each element of D($j\omega$) to a stable and minimum-phase transfer function D(s) and go to step 1.

The iteration continues until $\|DN(K)D^{-1}\|_\infty < 1$ or the $\mathcal{H}_\infty$ norm no longer decreases.

Using the derived $P - \Delta$ formulation, a controller can be designed with the DK-iteration method for robust stabilization. For the model being used and assuming a high rotating plasma, the growth rate γ ranges from 10 rad/s to 5,000 rad/s. This results in a range for the uncertain parameter c_{pp} that goes from 71 to 0.3325. This is the range of values for which the system should be stabilized so that the robust controller can be considered a suitable design.

The complete system that is used to design the controller has an additional two time delay blocks preceding the plasma model. The time delays physically represent the plasma control system and the power supply. For design purposes, the time delays are linearized using second order Padé approximations.

The controller is synthesized using the *dksyn* command in Matlab. During the process of synthesizing the controller, it is evident that controllers designed with a smaller, more unstable nominal c_{pp} value produce the widest range of stability for c_{pp}. This is because the normalized uncertainty δ is defined by a linear relationship with c_{pp}, while the unstable eigenvalue of the system is nonlinear with respect to c_{pp} (Fig. 2.2). Using a smaller, more unstable c_{pp} range, the defined linear relationship with δ more accurately represents the system by capturing the dynamics at the more

47

unstable values of c_{pp}. The DK controller is synthesized using a $P - \Delta$ system constructed for $c_{pp}^* = 0.39625$ ($\gamma^* = 3,722 rad/s$) and guarantees $\mu < 1$ for the range defined by

$$c_{pp_{min}} = 0.3325 \qquad c_{pp_{max}} = 0.46,$$

which is equivalent to

$$\gamma_{max} = 5,000 rad/s \quad \gamma_{min} = 2,903 rad/s.$$

However, these results are conservative and, as it will be shown in the next part, the stability and performance ranges for our system are indeed bigger. The conservatism is explained by the fact that the DK-iteration implicitly assumes that the uncertain parameter is complex and does not take advantage of the known phase information of the real uncertainty. As a result, the designed controller is more conservative, but the scaled singular value still converges such that $\bar{\sigma}\left(DND^{-1}(j\omega)\right) \leq 1$. The controller was simulated using the 15 eigenmode model with 36 states. The designed controller has an order of 108 and is reduced to an order of 16 before computing the effective stability and performance ranges.

3.2 NCF Model Based Controller

The normalized coprime factorization (NCF) controller is a frequency response controller used for non-parametric robust model-based control, compared to the DK-iteration controller which is a parametric approach. The NCF method depends heavily on loop shaping techniques of the original plant using the frequency response graphs (Fig. 2.13-Fig. 2.15). The desired performance is achieved by appending the original plant $G(s)$ with pre- (W_1) and post- (W_2) compensators. The compensators shape the open-loop plant $G(s)$ prior to controller synthesis, which allows

the closed-loop weighted system to achieve the performance specifications. In general the performance is characterized by shaping $G(s)$ such that the augmented plant $(G_s(s) = W_2 G(s) W_1)$ has large gain at frequencies of desired disturbance attenuation and small gain where robust stability is required. The weight W_2 is considered the output weight and for systems with multiple outputs, different constants can be used to emphasize the importance of one output over another. In the case of the RWM model, both the sine and cosine components of the output are equally important, thus the output weight is set to $W_2 = I_2$. The weight W_1 is considered the performance weight and is dependent on the shape of the loop transfer function and can take on a different shape for each input into the system. The general transfer function for the performance weight is

$$W_1 = \frac{(M^{-1/n} s + \omega_b^*)^n}{(s + \omega_b^* A^{1/n})^n}.$$

For the NCF controller design the augmented plant $G_s(s) = W_2(s) G(s) W_1(s)$ is used and the NCF algorithm determines the optimal $\mathcal{H}_\infty$ controller (K_∞) that minimizes the $\mathcal{H}_\infty$ cost functions:

$$\gamma_{ncf} := \min_{K_\infty} \left\| \begin{bmatrix} I \\ K_\infty \end{bmatrix} (I - G_s K_\infty)^{-1} [G_s, I] \right\|_\infty$$

$$\gamma_{ncf} := \min_{K_\infty} \left\| \begin{bmatrix} I \\ G_s \end{bmatrix} (I - K_\infty G_s)^{-1} [K_\infty, I] \right\|_\infty,$$

where γ_{ncf} is the optimal stability margin of the closed-loop system. By definition, γ_{ncf} is always greater than 1, however a smaller γ_{ncf} corresponds to a satisfactory stabililty margin. The NCF controller applied to the system $G(s)$ is defined as $K_{ncf} = W_1 K_\infty W_2$ [12]. The augmented plant $G_s(s)$ is used in the design to ensure that the $\mathcal{H}_\infty$ norm is less than 1 for all frequencies. This ensures that the original plant $G(s)$ will have the desired closed-loop shape as determined by the performance weights.

The NCF method takes the linear plant $G_s(s)$ and finds the coprime, normalized stable transfer functions M_s and N_s, such that $G_s(s) = M_s^{-1} N_s$. Introducing the uncertain parameters, the family of plants is given by

$$G_\epsilon = \left\{ (M_s + \Delta_{M_s})^{-1} (N_s + \Delta_{N_s}) \right\},$$

where

$$\|[\Delta_{M_s} \Delta_{N_s}]\|_\infty < \epsilon.$$

The designed stabilizing controller K_∞ ensures that the closed-loop system will remain stable for the uncertainty range given by ϵ. The stability margin and the range of uncertainty ϵ are related through $\frac{1}{\epsilon} = \gamma_{ncf}$.

After several controller design attempts by adjusting the variables and order (n) of the transfer function in the performance weight, it was determined that $n = 2$ provides the best performance weight for the system. After many different performance weight considerations and simulations, the final performance weights were chosen with the following parameters

$$M = 10^6$$

$$\omega_b^* = 10^7$$

$$A = 5 \times 10^{-5}.$$

The frequency response of this weighing function is seen in Fig. 3.1. The performance weight was applied equally to all three inputs into the system such that $W_1 I_3$ was the performance weight. This controller was designed using a c_{pp} value of 0.29 using the 29 eigenmode model with 64 states. The controller was designed with an order of 54, but using model reduction the order was reduce to 12 while maintaining similar performance characteristics.
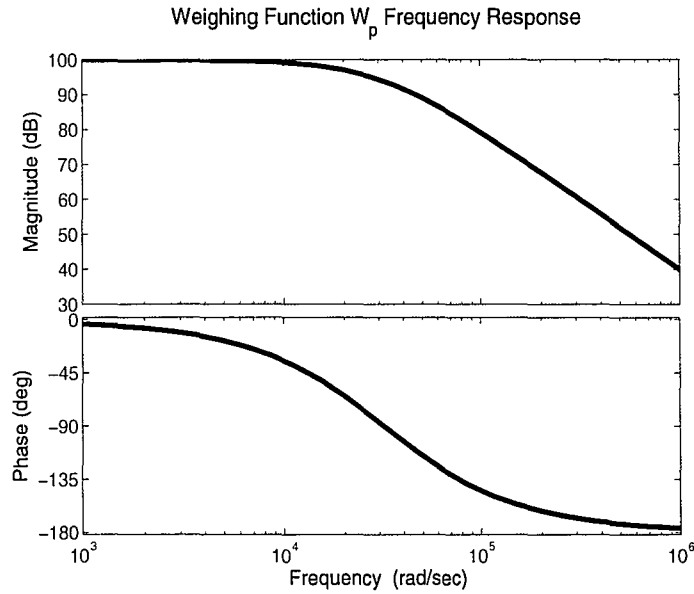
Figure 3.1: Frequency Response of the Weighing Function W_p

3.3 LQG Model Based Controller

The LQG controller is a combination of the linear quadratic regulator (LQR) state feedback matrix and a Kalman filter, which is a state estimator. The state feedback law is given by $u = -K\hat{x}$, where K is the state feedback gain matrix. This state feedback law minimizes the quadratic cost function,

$$J(u) = \int_0^\infty \left(\hat{x}^T Q \hat{x} + u^T R u \right) dt$$

where $\hat{x}$ is the Kalman state estimate and Q and R weighting matrices that weight the states and inputs respectively. The state feedback gain of the LQG controller is found by first solving the solution S of the associated Riccati equation

$$A^T S + SA - SBR^{-1}B^T S + Q = 0.$$

51

From the solution of the Riccati equation the controller is found by

$$K = R^{-1}B^{T}S.$$

The Kalman filter equation is,

$$\dot{\hat{x}} = A\hat{x} + Bu + L(y - C\hat{x})$$

where L is the filter gain matrix, which is found by solving the following algebraic Riccati equation for P,

$$0 = AP + PA^{T} + BQ_{n}B^{T} - PC^{T}R_{n}^{-1}CP$$

and inserting P into

$$L = PC^{T}R_{n}^{-1}$$

where Q_{n} and R_{n} are the process and sensor noise covariance matrices of the Kalman filter. The final controller is governed by the state-space equations

$$K_{LQG} : \begin{cases} \dot{\hat{x}} = [A - LC - BK]\hat{x} + Ly \\ u = -K\hat{x} \end{cases}$$

The same design parameters used in [13] were used, where the Q and R weighting matrices are diagonal matrices of 1.0×10^{-4} and 1.0×10^{8} respectively putting more weight on the inputs and less on the states. Also, the Q_{n} and R_{n} noise covariance matrices are given by 1.0×10^{8} and 1.0×10^{-4} respectively to decrease process noise and increase reliance on sensor noise. This controller was designed using a c_{pp} value of 0.29 using the 29 eigenmode model with 64 states. The controller was designed with an order of 74, but using model reduction the order was reduce to 8 while maintaining

52

similar performance characteristics.

3.4 LQRY Model Based Controller

The LQRY controller is very similar to the LQG controller design method. The only difference is in the application of the weights. Instead of applying the weights to the states of the system, the LQRY applies the weighting to the outputs of the system. Therefore, all of the above equations hold for the LQRY as well, except for the quadratic cost function is now defined as

$$J(u) = \int_0^\infty \left(y^T Q y + u^T R u \right) dt$$

where Q is now the weighting matrix of the outputs. All other definitions hold for the LQRY case, including the governing equation of the controller K_{LQRY}. For this case, the Q and R weighting matrices are diagonal matrices of 1.0×10^8 and 1.0×10^{-4} respectively putting more weight on the outputs and less on the inputs to increase bandwidth. The same noise covariance matrices are used as well. This controller was designed using a c_{pp} value of 0.29 with the 29 eigenmode model with 64 states. The controller was designed with an order of 74, but using model reduction the order was reduce to 11 while maintaining similar performance characteristics.

3.5 PD Performance Based Controller

A *PID* controller was designed to maximize the stability range of γ. It was determined that integral action is not required for this system, so using the standard implementation the *PD* controller is of the form

$$K_{ij} = \frac{G_{P_{ij}} + G_{D_{ij}} s}{1 + \tau_{pcs} s}$$

where i is the index for the control inputs into the system $(i = 1 \ldots 3)$, j is the index for the number system outputs $(j = 1 \ldots 2)$, G_P is the proportional gain, G_D is the derivative gain, and τ_{pcs} is the time constant taken to be 4×10^{-4} sec. Each K_{ij} term fills the 3×2 controller matrix K. To go about determining each entry into the K matrix, a stabilizing controller with $K_{11} = K_{22}$ and every other term set to zero was considered as a base case. After determining the stability range of this controller, these terms were held constant and the remaining terms were individually checked the maximum stability range under the optimal condition. The only term that had a more stabilizing effect was the K_{32} term. Using a controller with the terms K_{11}, K_{22}, and K_{32} all six gains were optimized to obtain the maximum range of γ for stability. This was done by holding two of the controller terms constant and sweeping the proportional and derivative gains for one controller term to determine the stability range of γ. After the gains were optimized for one controller term, the process was continued for the other two controller terms. The resulting gains are

$$G_{P_{11}} = 3.80 \times 10^4 \quad G_{D_{11}} = 76$$
$$G_{P_{22}} = 1.38 \times 10^4 \quad G_{D_{22}} = 40$$
$$G_{P_{32}} = 6.62 \times 10^4 \quad G_{D_{32}} = 103.$$

The maximum growth rate γ at which the system remains stable was found to be 5,980 rad/s. The γ contours that display the PD with respect to the growth rate γ can be seen in Fig. 3.2(a) for this design case. This figure assumes that the first two controller terms are fixed using the parameters given above, and the third controller term gains are scanned for stability. For each γ contour, the system is stable inside of the curve and unstable outside of the curve. The advantage of using three tunable controller terms instead of using the same gains for each term are shown in Fig. 3.2(b). This figure assumes that all three controller terms are equal to each other, and the gains are tuned for stability. It is easily seen that stability range is reduced to a maximum stable γ of 4,594 rad/s, with controller gains $G_P = 2.33 \times 10^4$ and

$G_D = 40$. The single term PD controller presented in [13] shown in (Fig. 3.3(a-b)) has better results than the single term PD controller designed for the updated model because that case considered a square model (either 2×2 or 6×6 system) which took advantage of every input and output of the system. Applying the same concept to a 3×2 model ignores the effect of the third input, which limits the ability of the controller to have good performance results. The single term PD from previous work [13] does not have as much range as the three term PD controller.
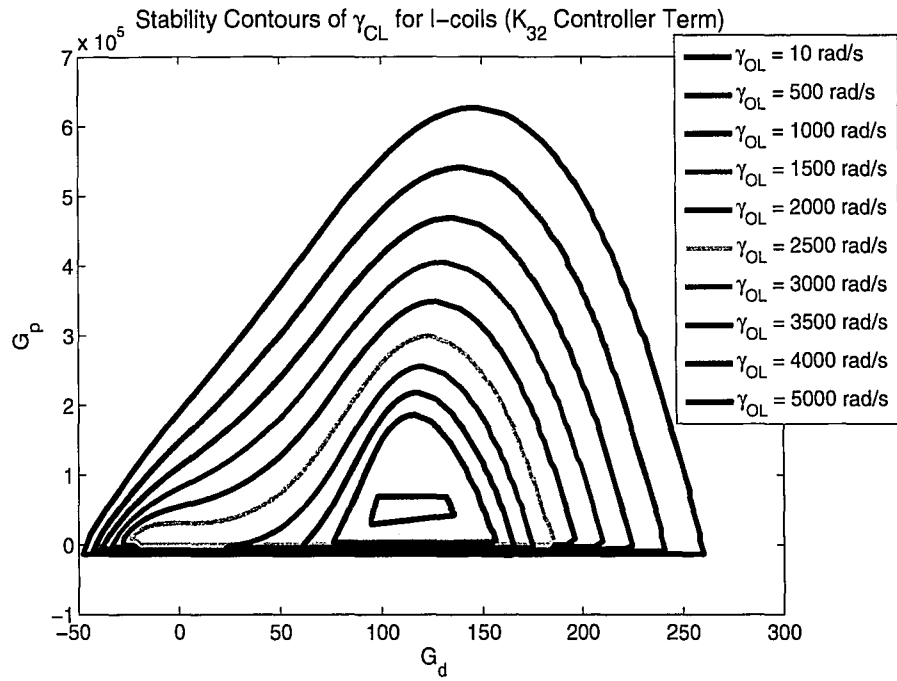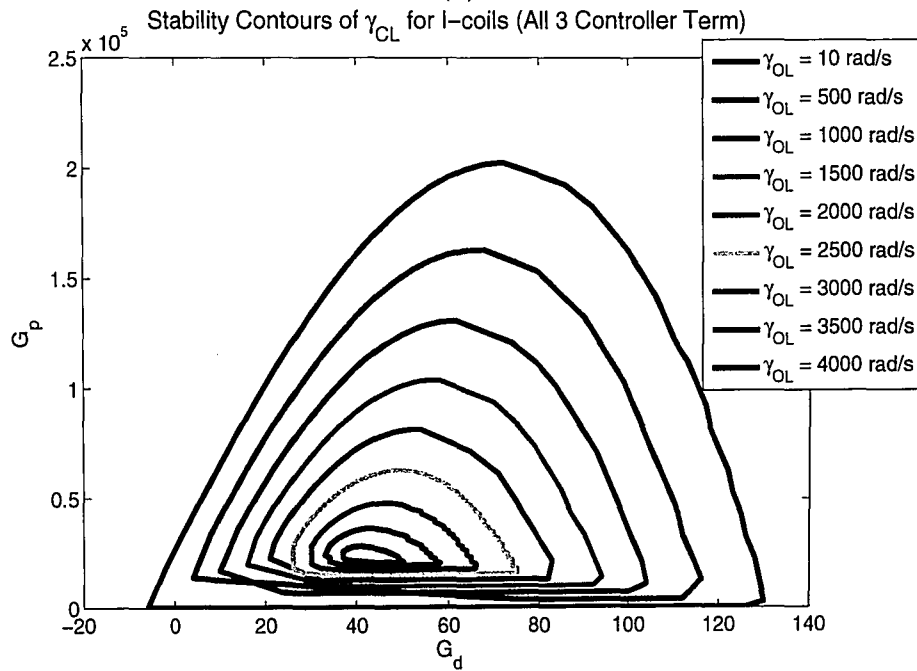
Figure 3.2: γ contours of stability for (a) Varying term PD, (b) Constant term PD.
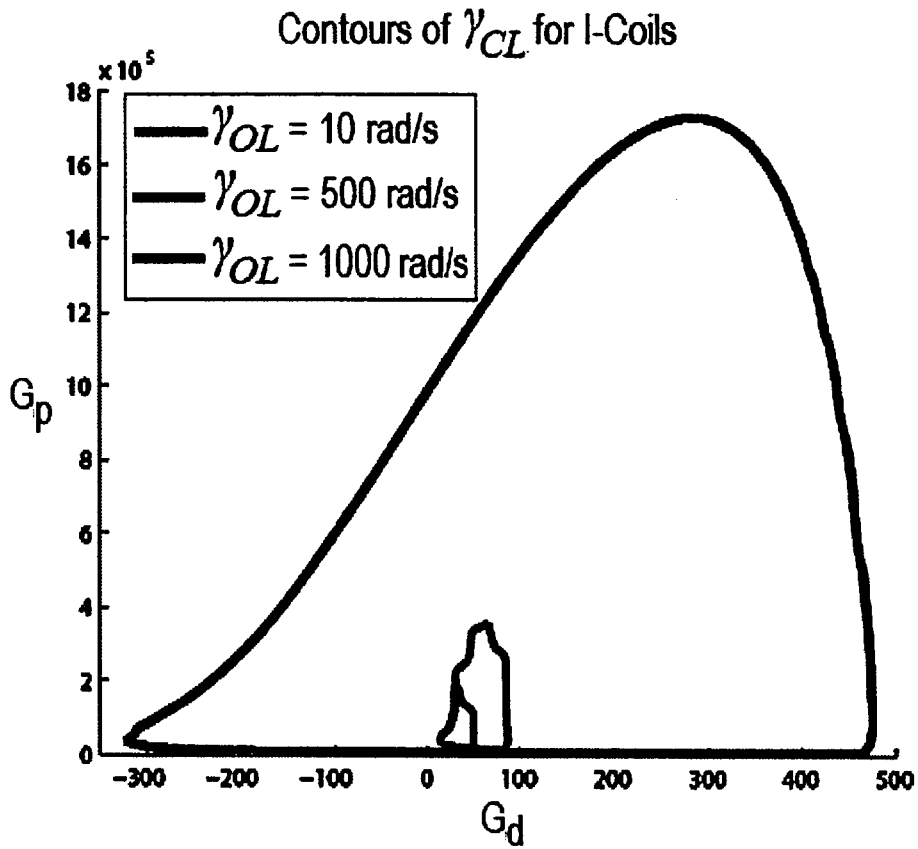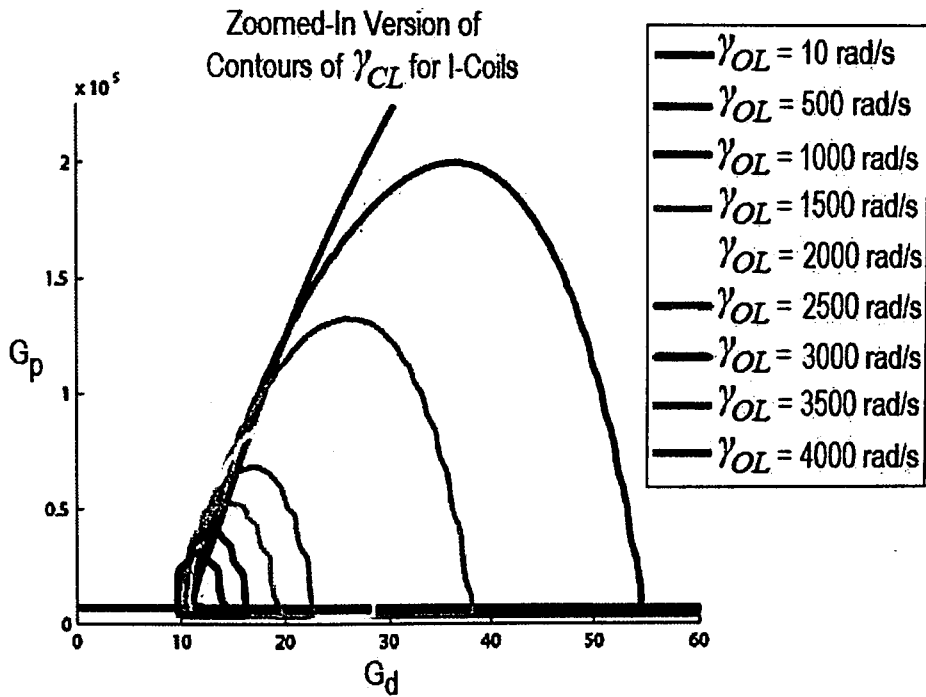
Figure 3.3: γ contours of stability for (a)-(b) [13] Results constant term PD.

Chapter 4

Controller Comparison

A useful comparison of controllers is to determine the range of γ where the system remains stable as well as a range where the system performs within the limits of the performance constraints. The five controllers compared in this part are the *LQG*, *LQRY*, *NCF*, *DK*, and *PD*. The desired range of stability for the growth rate γ is [10-5,000] rad/s, with a nominal value at 120 rad/s. All simulations in this chapter are performed using the 29 eigenmode model with 64 states. The performance targets and constraints are given in Table 4.1.

4.1 Simulink Model

The new Simulink model can be seen in Fig. 4.1. The plasma model block is the state space representation of the RWM plasma model altered to accept a time-varying value

Table 4.1: Performance Targets and Constraints

Condition	Target Value	Maximum Constraint
Rise Time	1.0ms	5.0ms
Settling Time	5.0ms	10ms
Overshoot	15%	50%
Input Voltage	N/A	± 100V

of c_{pp}. The input to the plasma model block is the 6 control voltages, of which the first 3 C-coil controls are set to zero. The output is the 23 sensor readings. The plasma model block can also add independent band-limited white noise to each of the 23 sensor outputs of the system if desired. The MF gain block is the matched filter that reduces the outputs to the two RWM mode amplitudes. The next series of blocks entering through the Switch determine the reference value of the RWM mode amplitude, either through initial condition response, an impulse response, or a step response. The controller block is the state space representation of the designed controller to be tested and the Switch1 determines whether a designed model based controller or the PD controller is used in the simulation. The pcs delay block is a pure delay of time constant 65×10^{-6} sec to represent the plasma control system operation. The RWM PS block is the power supply block which is represented by a saturation limit of $\pm 100V$, a pure delay of time constant 5×10^{-6} sec, and a transfer function $\frac{1}{4 \times 10^{-6} s + 1}$. The gains in the model are set to 1.

Three simulation profiles were created to test the controllers; an initial condition test, an impulse response test, and a step response test. The initial condition test initializes the plasma states to set the output RWM mode amplitude to a value of 1 Gauss for the simulation start time of $t = 0sec$. The reference value of RWM mode amplitude is set to zero. The impulse response test creates an impulse of 1 Gauss at a time of $t = 0.001sec$ and lasts for $0.0001sec$. The step response test creates a step of 1 Gauss starting at a time of $t = 0.001sec$.

4.2 Stability and Performance Ranges

4.2.1 Test Detail

Tables 4.2-4.3 provides the range of γ for which the model satisfies certain conditions. In Table 4.2 the first column *Order* is the order of the designed controller. The second
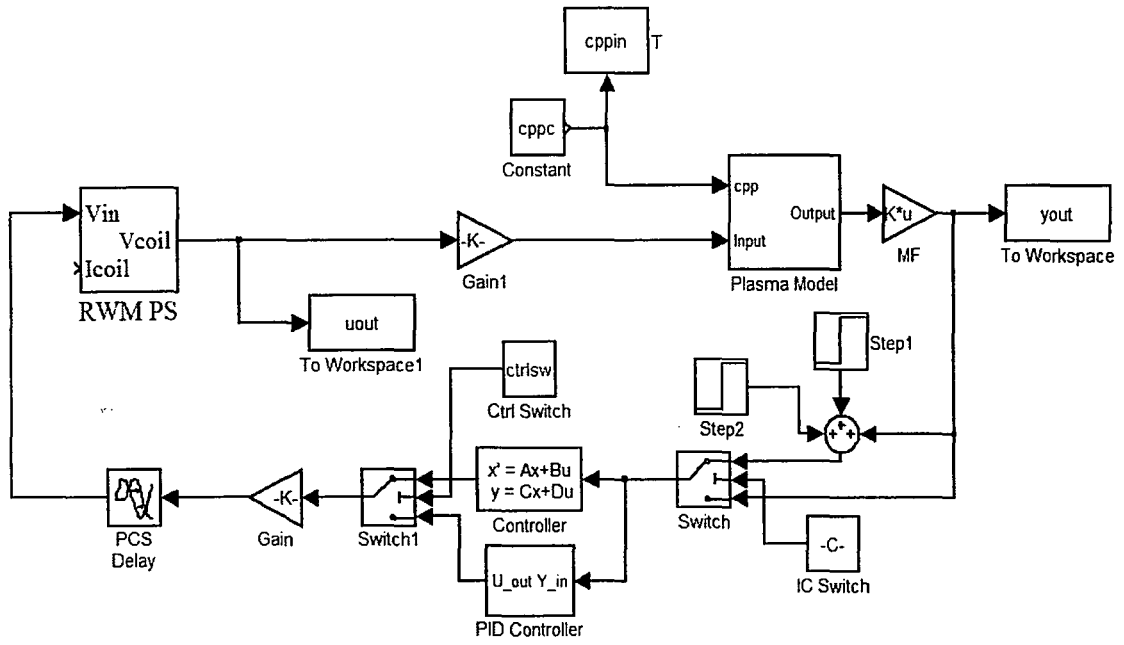
Figure 4.1: Simulink Model of the Control System and Plasma Model

Table 4.2: Stability Ranges

Controller	Order	Stability Range (Eigen.)	Stability Range (Step)
LQG	8	0 - 9,109 rad/s	0 - 9,100 rad/s
LQRY	11	0 - 8,514 rad/s	0 - 8,263 rad/s
NCF	12	0 - 9,027 rad/s	0 - 8,418 rad/s
DK	16	0 - 7,747 rad/s	0 - 7,437 rad/s
PD	2	0 - 5,980 rad/s	0 - 5,042 rad/s

column *Stability Range (Eigen.)* is the range of γ that stabilizes the system based on it's eigenvalues, using the Padé approximation for the time delays. The third column *Stability Range (Step)* indicates the range of γ for which the system remains stable when using a unit step input for the RWM mode amplitude. Table 4.3 represents the range of γ for which the performance conditions are satisfied under the same condition.

The ranges in Tables 4.4-4.5 are determined using an initial condition and an impulse response test in Simulink. Again, the stability limit is found by observing the divergence point of the response. The initial condition response simulates the closed-

60

Table 4.3: Performance Ranges

Controller	Performance Range (Step)
LQG	0 - 7,694 rad/s
LQRY	0 - 7,628 rad/s
NCF	0 - 8,418 rad/s
DK	0 - 7,254 rad/s
PD	0 - 2,247 rad/s

Table 4.4: Initial Condition and Impulse Stability Range

Controller	Stability Range (Both)
LQG	0 - 9,109 rad/s
LQRY	0 - 8,514 rad/s
NCF	0 - 9,027 rad/s
DK	0 - 7,747 rad/s
PD	0 - 5,980 rad/s

loop system without a reference value and with an initial RWM mode amplitude of 1 Gauss. The initial RWM mode amplitude level depends on the initial conditions assigned to the states of the system. The initial condition of the states are set by finding the unstable eigenvector of the system for a certain growth rate γ and scaling the eigenvector to match the desired 1 Gauss RWM mode amplitude. The impulse response simulates the closed-loop system where the reference value is an impulse of 1 Gauss for 0.1 ms. The performance range is determined by the condition that the RWM mode amplitude is reduced to two percent of it's maximum value by 10 ms from the beginning of the simulation.

4.2.2 Results

The results in Tables 4.2-4.3 are a good initial indicator of the advantage of model based controllers. Although the PD controller is a much smaller order controller, the stability range is not as robust as the other controllers despite covering the entire

Table 4.5: Initial Condition and Impulse Performance Range

Controller	Performance Range (Initial)	Performance Range (Impulse)
LQG	0 - 7,969 rad/s	0 - 8.340 rad/s
LQRY	0 - 8,113 rad/s	0 - 8,263 rad/s
NCF	0 - 8,746 rad/s	0 - 8,832 rad/s
DK	0 - 6,459 rad/s	0 - 7,314 rad/s
PD	0 - 3,278 rad/s	0 - 4,927 rad/s

desired range of growth rate $\gamma = [10 - 5,000]rad/s$. More importantly, the PD controller does not satisfy the performance conditions to a step response over the desired range of growth rate, while the model based controllers all meet performance criteria at $\gamma = 7,000rad/s$. The LQG controller is the smallest order controller of those meeting all of the conditions and it also has the widest stability range. The NCF controller has the widest performance range for the step response.

Similar to the previous tables, the Tables 4.4-4.5 performance ranges prefer the model based controllers. This table shows the performance response to the initial condition and impulse tests. Once again, the NCF controller has the widest range of performance for these two tests, while the PD does not fall into the desired range. The stability range exactly correlates with that predicted by Matlab in the previous table.

4.3   Step Response

4.3.1   Test Detail

Table 4.6 provides information about the performance of the controllers in response to a 1 Gauss step input function of the RWM mode amplitude. The first and second columns $S\text{-}S$ offset at $\gamma = 5,000$ rad/s and $S\text{-}S$ offset at $\gamma = 120$ rad/s are the steady-state offset values of the system response at the given value of γ. The third column

62

Table 4.6: Step Information

Controller	S-S offset at $\gamma = 5,000$	S-S offset at $\gamma = 120$	$\pm 10\%$ of 1 G Range
LQG	1.1375 G	0.0193 G	0 - 647 rad/s
LQRY	1.6062 G	0.0224 G	0 - 596 rad/s
NCF	1.4425 G	0.0216 G	0 - 596 rad/s
DK	2.473 G	0.0230 G	0 - 521 rad/s
PD	N/A	0.0349 G	0 - 361 rad/s

$\pm 10\%$ *of 1 G Range* is the range of γ values where the step function final value resides within $\pm 10\%$ of the 1 Gauss input.

4.3.2 Results

The *LQG* has the best performance under all of these conditions, closely followed by the *NCF*, *LQRY*, and *DK* controller. Although the *PD* controller does not have the stability and performance range that the other two have, the steady-state offset and step range is comparable to that of the model based controllers. Since the system does not have a pole located at the origin (integrator), for a step input there exists an error constant that determines the steady state offset. The steady state error increases under all controllers with increasing growth rate γ. As γ increases, the system dynamics of the open-loop system changes, which increases the error constant of the system.

4.4   Initial Condition Response

4.4.1   Test Detail

The initial conditions are calculated to have a RWM mode amplitude of 1 Gauss at the simulation starting time for a certain γ. As explained earlier, the initial RWM mode amplitude level depends on the initial conditions assigned to the states of the system.

Table 4.7: Varying Initial Conditions in γ

Controller	Saturation
LQG	24.05 rad/s
LQRY	25.05 rad/s
NCF	26.14 rad/s
DK	15.75 rad/s
PD	13.55 rad/s

The initial condition of the states are set by finding the unstable eigenvector of the system for a certain growth rate γ and scaling the eigenvector to match the desired 1 Gauss RWM mode amplitude. This growth rate γ that determines initial conditions of the states is set to a value of $\gamma = 120 rad/s$. Thus, if the initial condition response simulation is run using a growth rate of $\gamma = 120 rad/s$, the RWM mode amplitude would have a starting value of 1 Gauss. The *Saturation* column provides the minimum γ where the voltage saturation limit is first reached by the spike in the control voltage (Table 4.7).

4.4.2 Results

When the initial condition response simulation is run with a larger growth rate than $\gamma = 120 rad/s$ the resulting initial value of the RWM mode amplitude is less than 1 Gauss which results in less required control voltage. However, when the simulation growth rate is decreased below $\gamma = 120 rad/s$ the resulting initial value of the RWM mode amplitude is increased above 1 Gauss. Thus, the smaller reported growth rates in Table 4.7 correlate to wider ranges where the control voltages do not saturate. The *PD* controller performs the best in this condition, closely followed by the *DK* controller.

Table 4.8: Saturation Limits

Controller	Initial Condition	Step	Impulse
LQG	4.7 G	3.5 G	3.2 G
LQRY	4.6 G	3.5 G	3.3 G
NCF	4.4 G	4.0 G	3.7 G
DK	6.7 G	7.5 G	7.5 G
PD	5.2 G	5.7 G	5.7 G

4.5 Saturation Limits

4.5.1 Test Detail

Table 4.8 reports the maximum value of the RWM mode amplitude assumed by the specific test before saturation is reached in the control voltage. All of the simulations and initial conditions are designed using $\gamma = 120$ rad/s. The limits were found for each of the three test simulations and the values are reported in Gauss.

4.5.2 Results

One noticeable behavior is the ability of the DK controller to suppress the RWM mode amplitude at higher initial values without reaching the saturation of the coil voltages. In general, this behavior is directly related to the gain of the controller, which is inversely related to the stability and performance range for c_{pp}. The saturation limit provides a measure of the controller's ability to provide mode suppression at a given RWM mode amplitude without causing the maximum voltage to be applied to the coils.

Table 4.9: Noise Tolerance Levels

Controller	RMS Noise ($\gamma = 5,000$ rad/s)
LQG	8.97 G
LQRY	9.07 G
NCF	11.53 G
DK	15.12 G
PD	1.16 G

4.6 Noise

4.6.1 Test Detail

As a final check of the controllers, noise was added to the system to observe the predicted effect that it will have on the system. Only the sensor noise was taken into account, ignoring the process noise. The *Band-Limited White Noise* block in Simulink was used, which allows you to set the noise power and the sampling time. The sampling time was set to 5×10^{-6} sec. There are 23 noise blocks added to the simulation model to represent each of the 23 sensors in the system.

A test was performed to find the RMS noise level of the RWM mode amplitude that can be sustained until instability is reached. Table 4.9 summarizes the approximate RWM mode amplitude noise level at which this occurs. The column *RMS Noise* ($\gamma = 5,000$ *rad/s)* corresponds to an initial condition response test at a growth rate of $\gamma = 5,000$ rad/s to determine the maximum noise level before instability was reached. For all simulations, the sampling time of the simulation is equal to the sampling time of the noise blocks.

4.6.2 Results

The *LQRY*, *NCF*, and *LQG* can withstand a large amount of noise amplitude, but the *DK* can withstand the most noise. One thing to note is that the time range used

66

in the simulations of these test was from 0-15 ms. This time range restricts the ability to confidently report the maximum allowable RMS noise. Once the reported noise level is reached, the controller starts using bang-bang control, which can only stabilize the system for a short period of time before control is completely lost. The reported noise level corresponds to a system that is stable within a 0-15 ms time range, however it could go unstable after this time. An example of saturation causing instability is in Fig. 4.2(c-d). This figure is the *LQG* controller response to initial conditions of 1 Gauss at $\gamma = 5,000$ rad/s. An example of a stable response to noise is shown in Fig. 4.2(a-b). This figure is the *LQG* controller response to initial conditions of 1 Gauss at $\gamma = 5,000$ rad/s. The default noise value was used to produce an equivalent RMS noise level of 0.15 Gauss.

4.6.3   Frequency Response and Noise Spectrum

Fig. 4.3-4.4 provide the frequency response of the controllers as well as the noise spectrum. Despite all of the different characteristics of the controllers, the one similarity between them is the approximate value of the cutoff frequency at $10^4 rad/s$. The noise spectrum was implemented to have a wider frequency range up to approximately $10^6 rad/s$. This is to help improve the accuracy of the results of the noise simulations by using a sampling time much smaller than the fastest dynamics of the system, which are introduced through the controller.
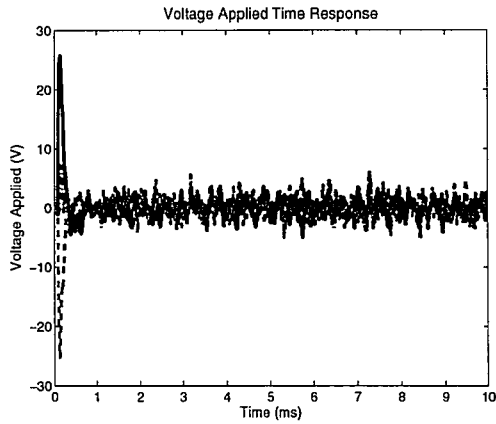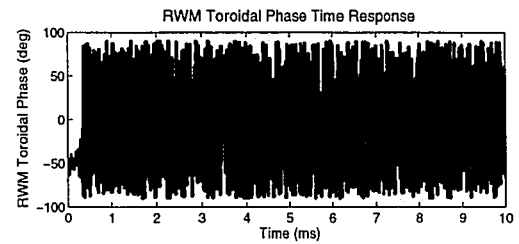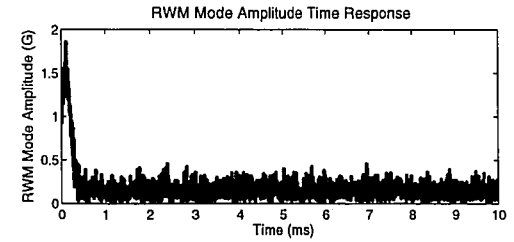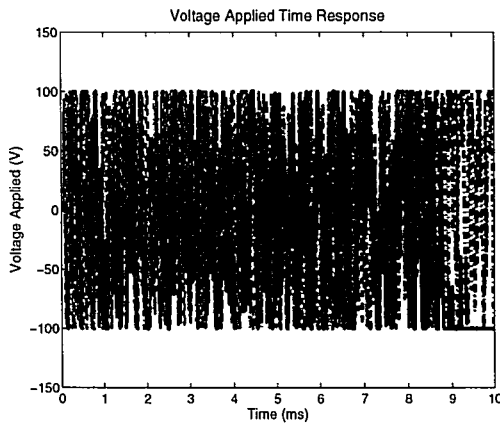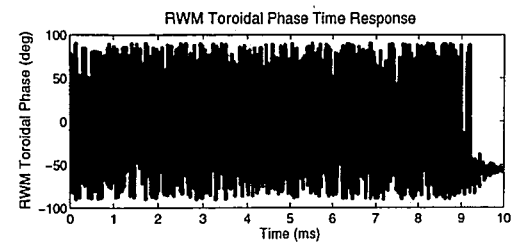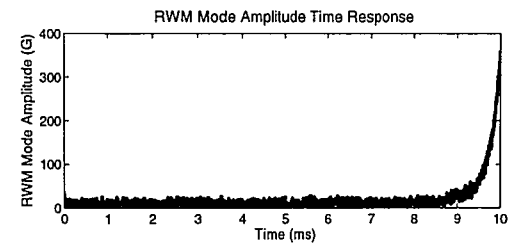
Figure 4.2: LQG response to initial conditions for $\gamma = 5,000$ with noise (a-b) Stable Case and (c-d) Unstable Case.
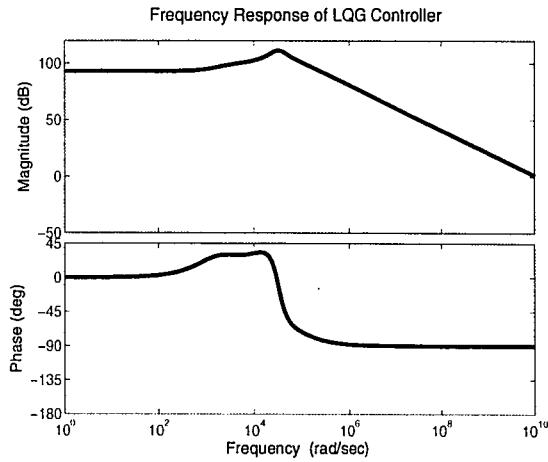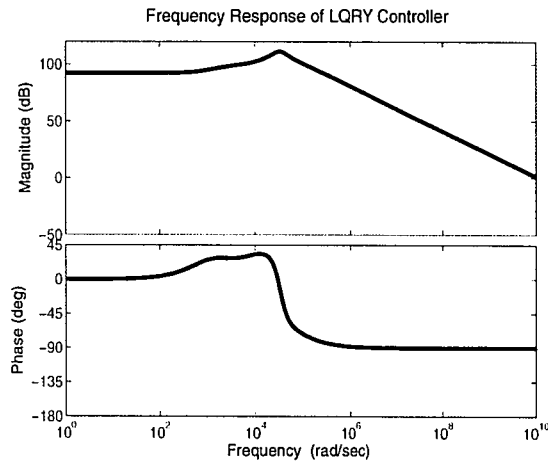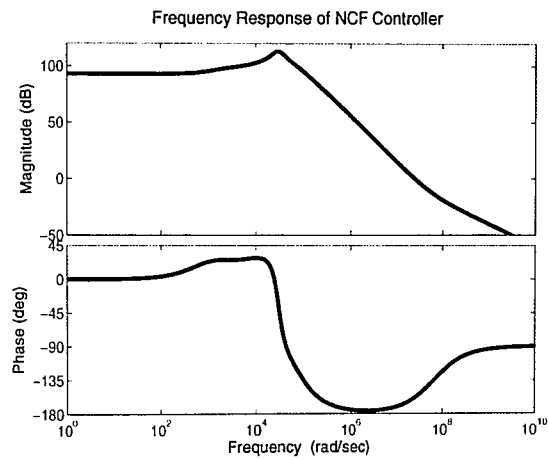
Figure 4.3: Frequency Response for (a) LQG, (b) LQRY, and (c) NCF.
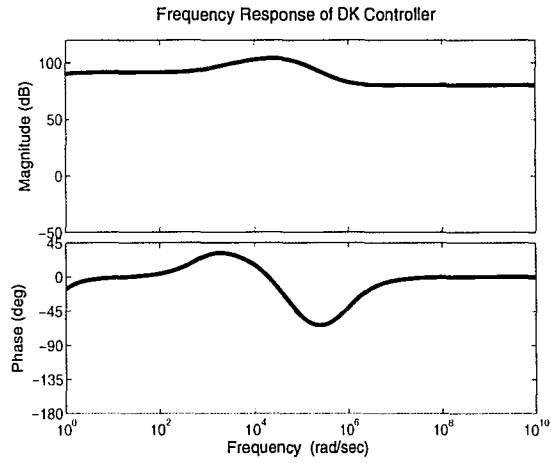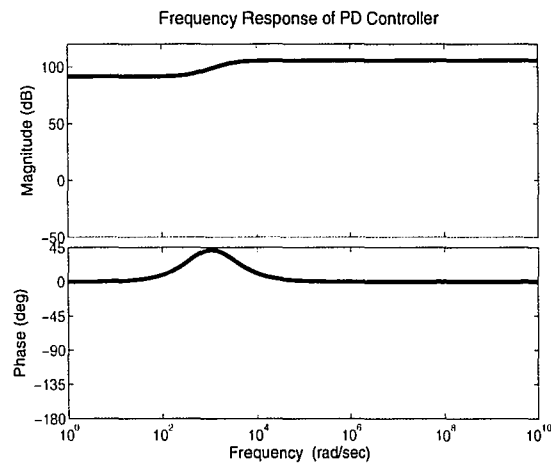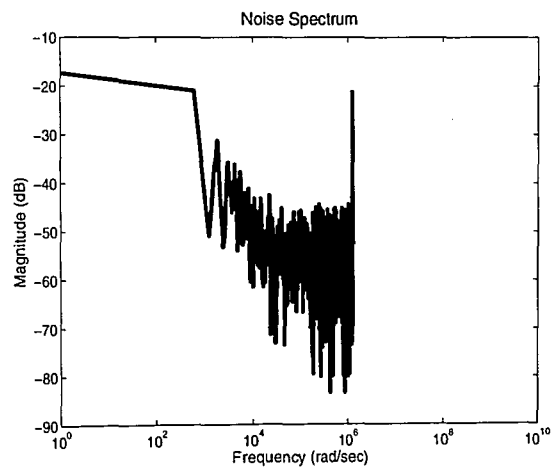
Figure 4.4: Frequency Response for (a) DK, (b) PD, and (c) Noise Spectrum.

4.7 Comparison with Controllers Designed in Previous Work

4.7.1 Test Detail

The next step is to compare the above results with the stability and performance ranges determined in previous control design efforts from [13]. Although it is useful to compare the ranges of growth rate, there are several key differences to note. First of all, these results do not take into account the changing value of c_{pp} in the state-output matrix C. This causes inaccurate results when performing a robustness sweep of the system to determine the allowable range of γ in terms of system stability and performance. In addition, the model sizes are different as [13] used models that were 2×2 and 6×6 models, while this research uses a 3×2 model with a quartet configuration. Also, since these efforts were performed, updated models that incorporate the additional line resistances and inductances have been created to more accurately represent the operation of DIII-D.

Table 4.10 provides a comparison of previous results from [13] with the new design results from this research. The controller designs from [13] were designed and tested on three different models, and this table reports the widest stability and performance ranges of each controller out of all three models. The results in the *New Design Results* column are from simulations where the reported stability and performance ranges are in response to a 1 Gauss step input.

4.7.2 Results

This table shows that using the updated models, including the state-output dependency on c_{pp}, and using a quartet configuration improve the stability and performance range of both the model based controllers and the performance based PD controller.

Table 4.10: Growth Rate Comparison

Controller	Previous Design Results		New Design Results	
	Stability	Performance	Stability	Performance
LQG	10 - 7,200 rad/s	500 - 4,550 rad/s	0 - 9,100 rad/s	0 - 7,694 rad/s
LQRY	10 - 2,000 rad/s	10 - 1,700 rad/s	0 - 8,263 rad/s	0 - 7,628 rad/s
NCF	10 - 4,550 rad/s	30 - 3,200 rad/s	0 - 8,418 rad/s	0 - 8,418 rad/s
DK	–	–	0 - 7,437 rad/s	0 - 7,254 rad/s
PD	10 - 1,800 rad/s	200 - 1,300 rad/s	0 - 5,042 rad/s	0 - 2,247 rad/s

The growth rate ranges for stability and performance have been increased greatly. The design goal mentioned in the thesis [13] was that the PD controller gains were chosen primarily based on the performance results, which greatly reduced the stability range of the controller. It is reported that a PD controller with a stability range of $\gamma = [10, 4100]$ rad/s could be obtained, however this controller does not satisfy the performance constraints. The main design goal of the recently designed PD controller was to maximize the range of stability and determine the performance range afterwards. The differences in the PD performances and stability ranges is due to the differences in the models described above.

4.8 Response Graphs

4.8.1 Test Detail

The following pages contain the system response to several different conditions. For all of the figures, the following subfigures show: (a) c_{pp} and γ time profiles, (b) LQG response, (c) $LQRY$ response, (d) NCF response, (e) DK response, and (f) PD response. Fig. 4.5-4.7 show the initial condition responses of the RWM mode amplitude for $\gamma = 10 rad/s$ ($c_{pp} = 71$), RWM mode amplitude for $\gamma = 5,000 rad/s$ ($c_{pp} = 0.3325$), and the applied control voltages for $\gamma = 5,000 rad/s$ ($c_{pp} = 0.3325$) respectively. Fig. 4.8-4.9 show the RWM mode amplitude response to a unit step for

$\gamma = 10rad/s$ and $\gamma = 5,000rad/s$ respectively. Since the robust controller stabilizes the plant over a range of growth rate, it is of interest to investigate the controller performance using time-varying of growth rate γ. The results for ramping, stepping, and sinusoidal functions of the c_{pp} parameter are presented (Fig. 4.10-4.12). The ramp and step functions begin at an initial value of $\gamma = 120$ rad/s ($c_{pp} = 5.75$). The sinusoidal function is defined by the design range of γ of the controller with a frequency of 5,000 rad/sec. Finally, one case is shown where noise included in the sensor signal readings (Fig. 4.13). The sensor noise is assumed to have a sampling time $T_s = 5 \times 10^{-6}sec$ and a RMS noise level of 0.15 Gauss.

4.8.2 Results

The initial condition response at the slow end of the growth rate range shown in Fig. 4.5 has satisfactory results for all of the designed controllers. The LQG, $LQRY$, NCF, and DK controllers all have quick suppression of the RWM mode amplitude within 1.5 ms. The PD controller uses more effort to suppress the mode, taking approximately 2.5 ms to settle.

For the faster growth rate shown in Fig. 4.6, there is some performance separation between the controllers. The $LQRY$ and NCF controllers provide the quickest mode suppression on the order of 1.5 ms, similar to that of the slower growth rate. The LQG also provides sufficient mode suppression within 3.5 ms. The DK controller allows the RWM mode amplitude to exist at a larger magnitude than the other model based controllers, however the mode is still suppressed within 3.0 ms. The PD controller has much more difficulty at higher growth rates and does not completely eliminate the RWM mode amplitude within the performance criteria, however does stabilize the system at high end of the growth rate range. An important variable to track in the stabilization of the RWM in the tokamak plasma is the applied control voltage to the coils. The voltage response for the fast growth rate initial condition response is

shown in Fig. 4.7. The LQG, $LQRY$, and NCF have similar control voltage profiles, a fast application that peaks with an absolute value of approximately 25 volts and goes to zero within 2 ms. The DK controller uses less applied peak voltage of 19 volts to suppress the RWM mode amplitude, yet the mode suppression is not a fast as the other model based controllers. The PD controller uses much more controlling action with a peak on the magnitude of 50 volts and much longer settling time.

The LQG, $LQRY$, and NCF controllers have similar responses to a unit step of the RWM mode amplitude at the lower growth rate of $\gamma = 10rad/sec$ (Fig. 4.8). These controllers have no overshoot and the settling time for these controllers is within a few tenths of a millisecond of the onset of the step function. The DK and PD controllers have approximately 15% overshoot and settles within 1.5 ms.

A unit step simulation at the faster growth rate of $\gamma = 5,000rad/sec$ reveals the different characteristic of the controllers (Fig. 4.9). The LQG controller has little overshoot, a settling time of approximately 3.5 ms, and the smallest steady state error (approximately 1 Gauss) of all the controller responses. The $LQRY$ controller has negligible overshoot, a fast settling time of 1.0 ms, and a steady state error above 1.5 Gauss. The NCF controller has approximately 10% overshoot, a settling time of 2.0 ms, and a steady state error under 1.5 Gauss. The DK controller has a much more oscillatory response with less than 10% overshoot, a settling time of approximately 3.5 ms, and a much larger steady state error of 2.5 Gauss. Finally, the PD is unstable for a step response at the fast growth rate.

For the results with time-varying growth rate, the ramping c_{pp} profile of Fig. 4.10 produces similar responses to that of the initial condition response with a slow growth rate. All of the controllers provide quick suppression of the RWM mode amplitude, while the PD uses more effort to eliminate the presence of the RWM.

The results in Fig. 4.11 provide insight into the controller behavior to large, instantaneous changes in the RWM growth rate. The c_{pp} profiles jumps between the

upper and lower limits of the desired range and the nominal value. The change in growth rate that caused the largest effect in RWM mode amplitude was from the fast growth rate to the slow growth rate. Due to the longer time for mode suppression at the faster growth rate, when the system was altered with the change in growth rate, the states of the system (currents in the conductor) were not completely at equilibrium ($x = 0$). The model based controllers were able to stabilize the system despite this large spike in RWM mode amplitude. The LQG was least effected by the change in growth rate, with a peak of 10 Gauss in the RWM mode amplitude and the fastest response of RWM mode suppression. The $LQRY$ and NCF controllers had similar response with a peak of 15 Gauss and a quick elimination of the RWM. The DK was effected the most by the changing growth rate with a peak of 25 Gauss and a longer settling time. The PD controller was unable to remain stable under the c_{pp} time profile.

For the sinusoidal time profile of c_{pp} (Fig. 4.12) the LQG, $LQRY$, NCF, and DK controllers provide fast control of the RWM within 2.5-3.0 ms. The performance based PD controller does stabilize the system, however has difficulty in completely eliminating the RWM under this condition. Fig. 4.13 displays the effect of noise on the controller responses. In general the model based controllers are able to take advantage of the modeled system dynamics to extend the stability and performance ranges of the driving instability term γ.
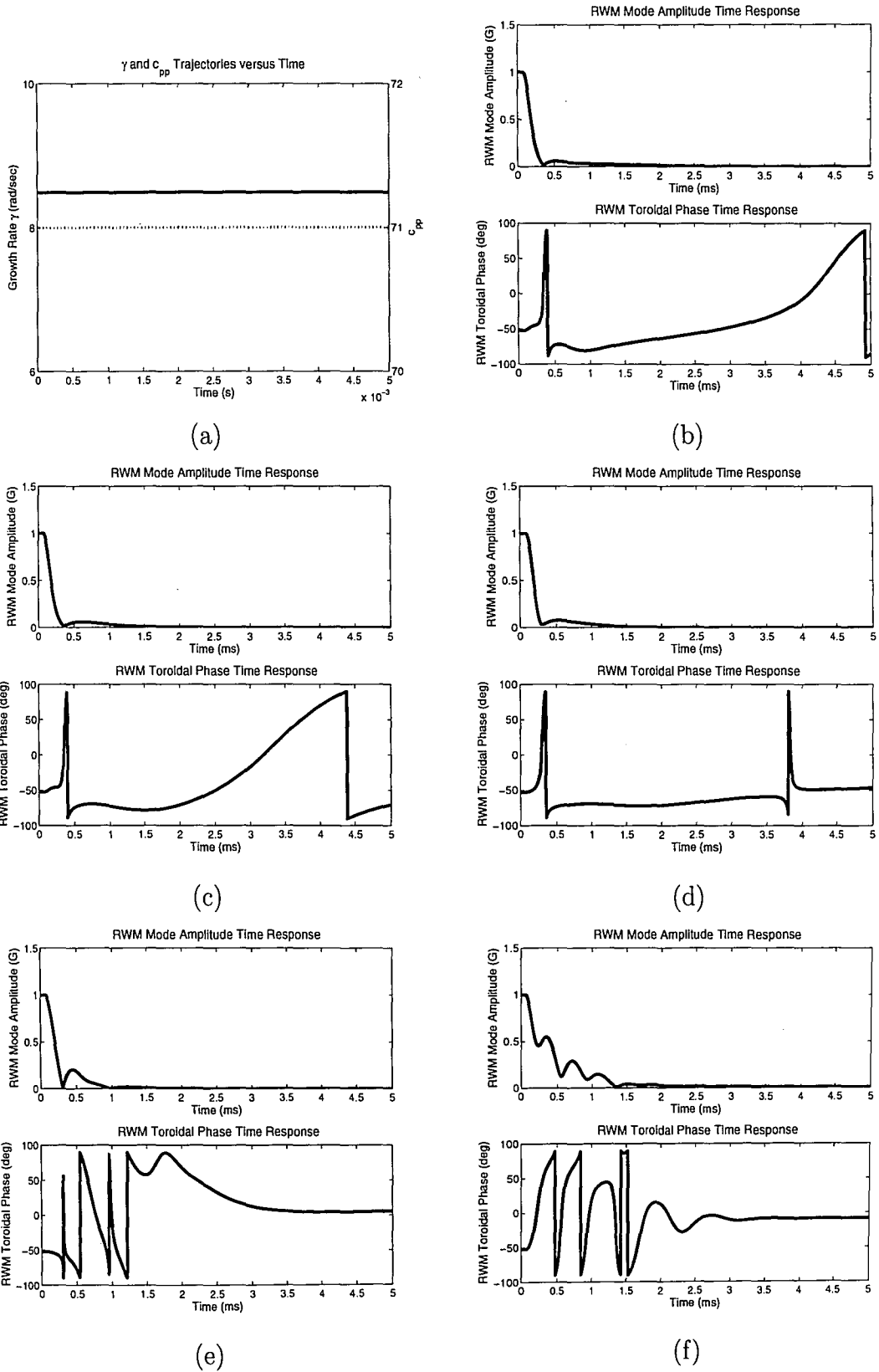
Figure 4.5: RWM response to initial conditions at (a) $\gamma = 10$ rad/s for (b) LQG, (c) LQRY, (d) NCF, (e) DK, and (f) PD.
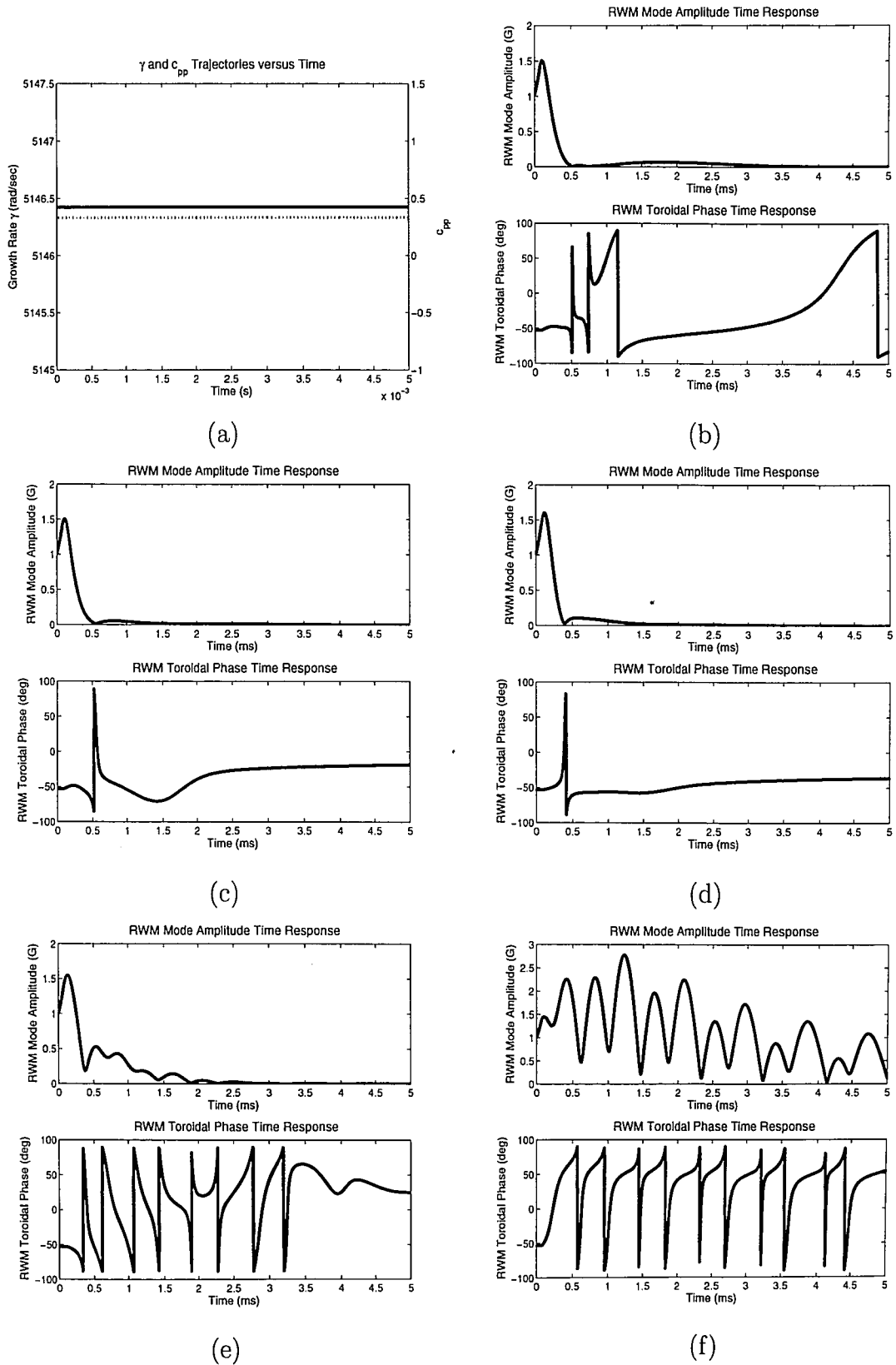
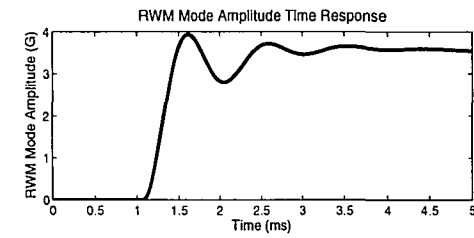Figure 4.6: RWM response to initial conditions at (a) $\gamma = 5,000$ rad/s for (b) LQG, (c) LQRY, (d) NCF, (e) DK, and (f) PD.

77
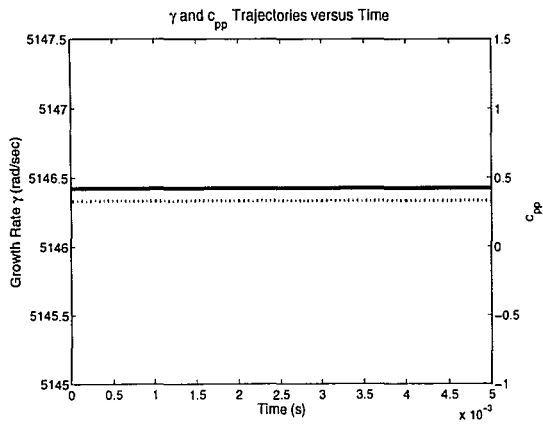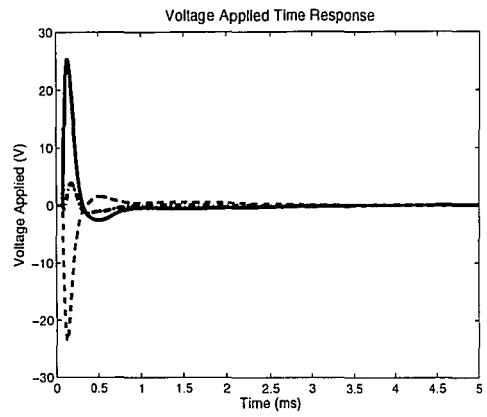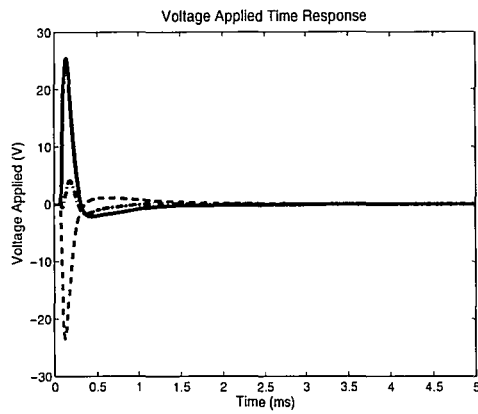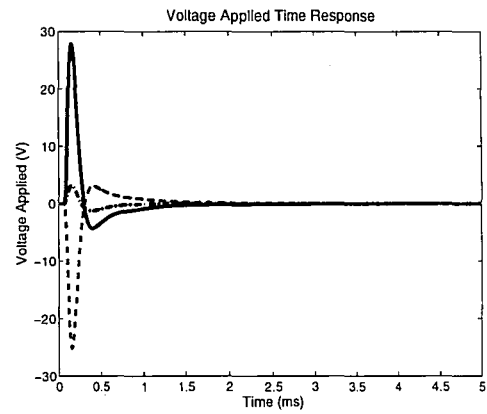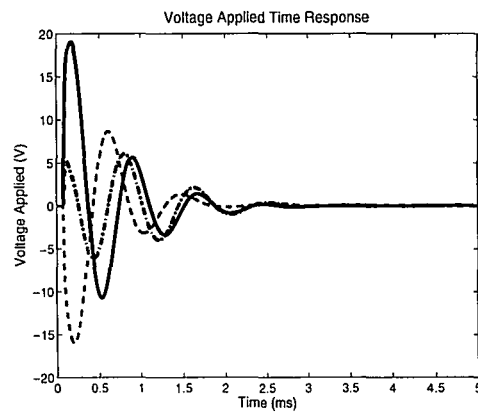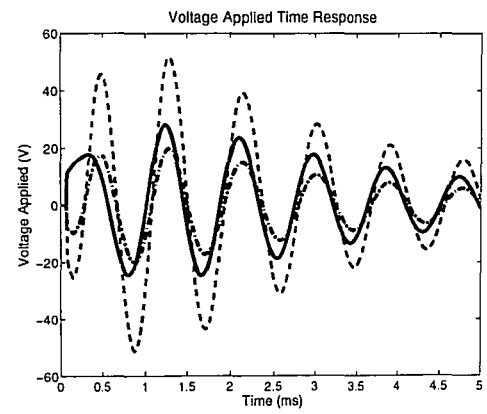
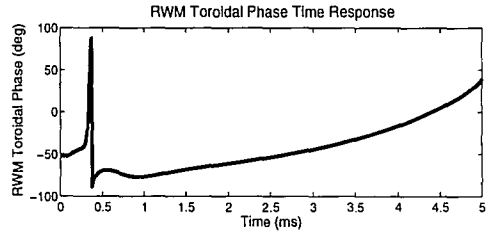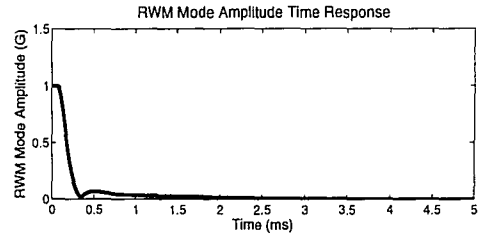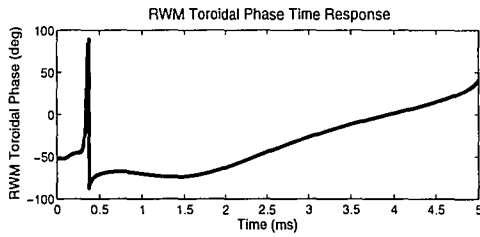Figure 4.7: Control Voltage response to initial conditions at (a) $\gamma = 5,000$ rad/s for (b) LQG, (c) LQRY, (d) NCF, (e) DK, and (f) PD.
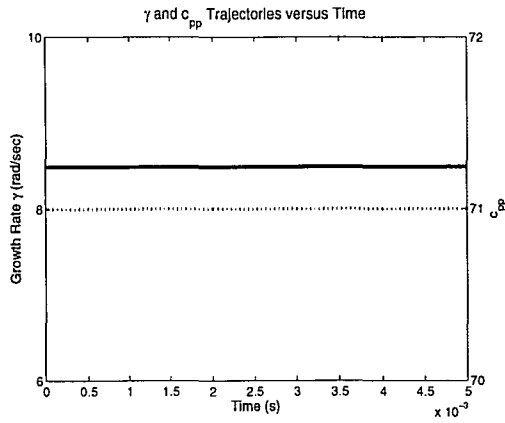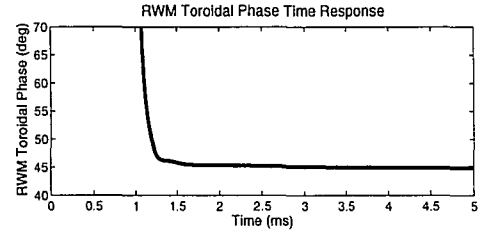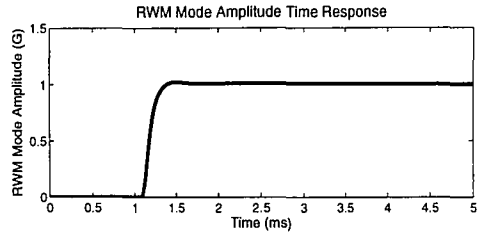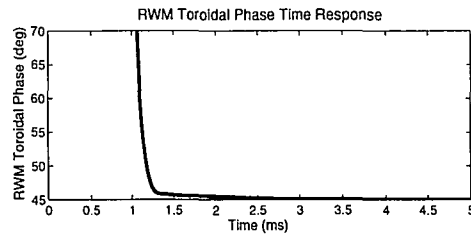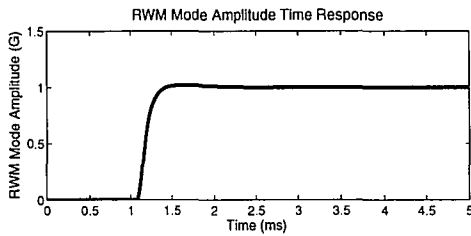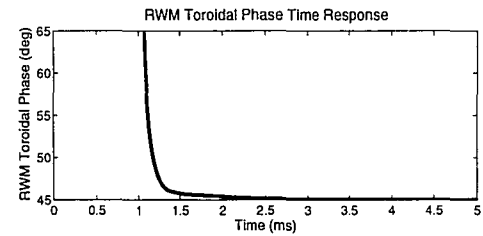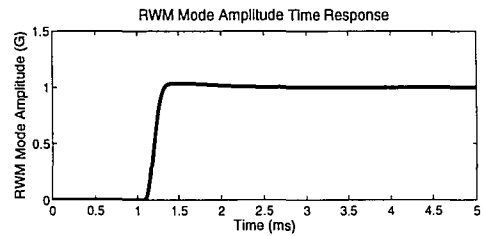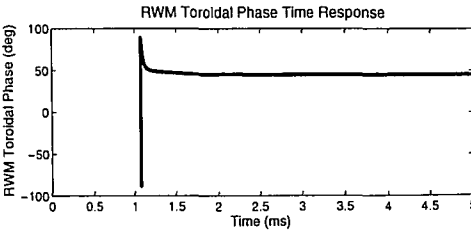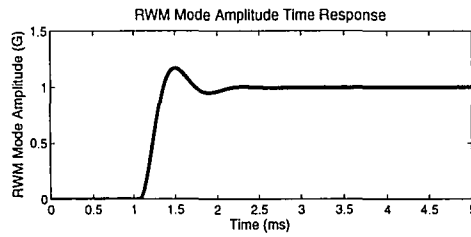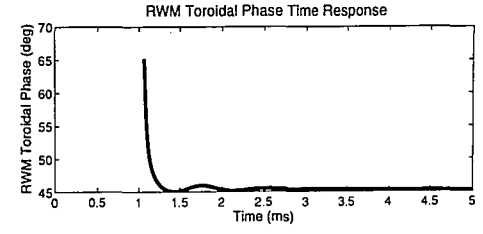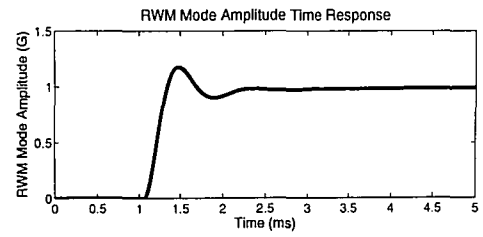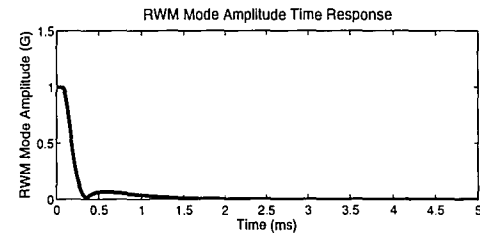
Figure 4.8: RWM response to unit step at (a) $\gamma = 10$ rad/s for (b) LQG, (c) LQRY, (d) NCF, (e) DK, and (f) PD.
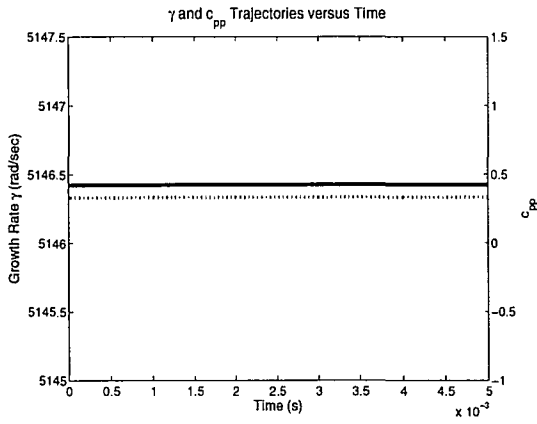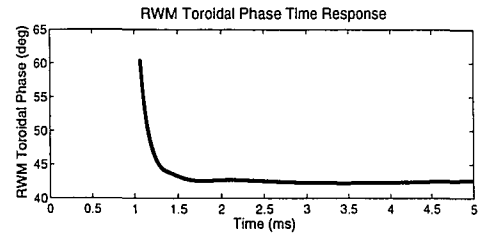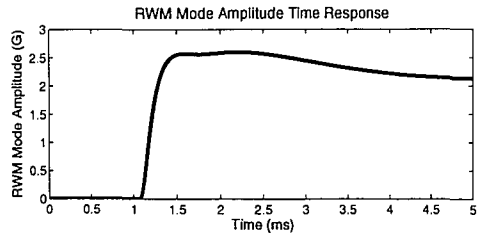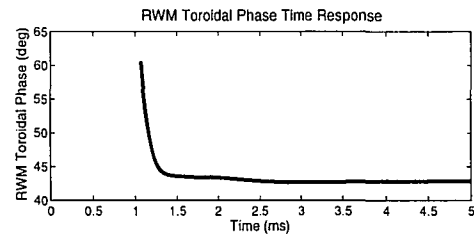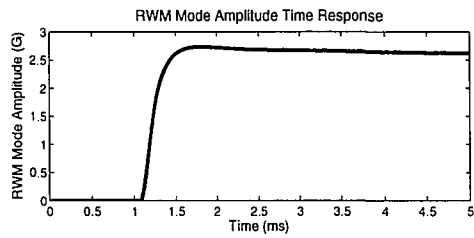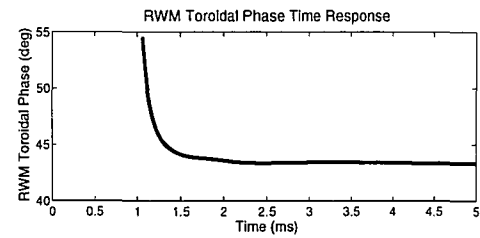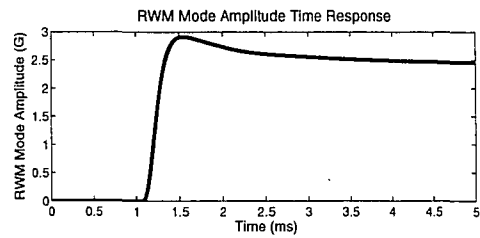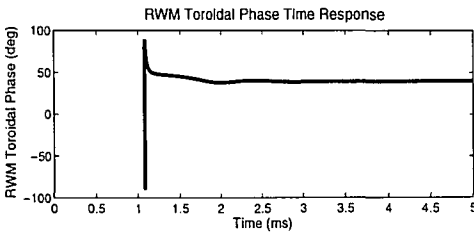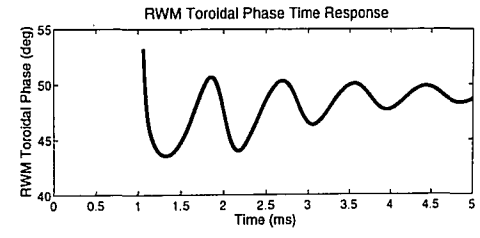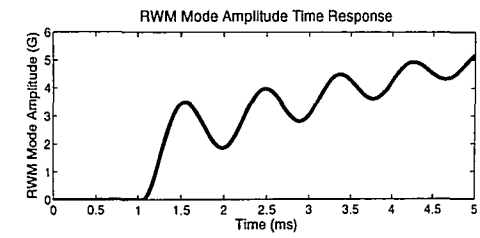
Figure 4.9: RWM response to unit step at (a) $\gamma = 5,000$ rad/s for (b) LQG, (c) LQRY, (d) NCF, (e) DK, and (f) PD.
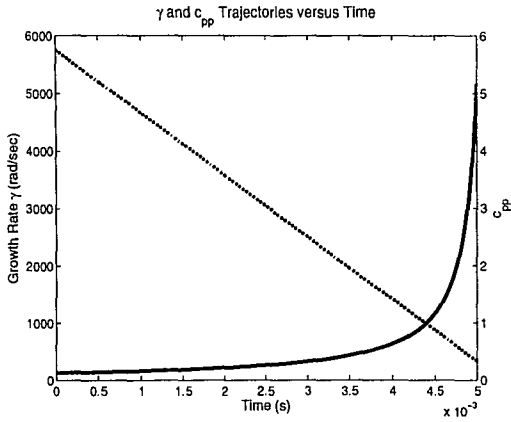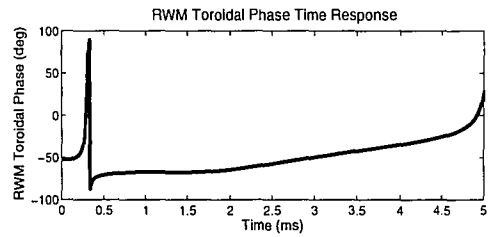
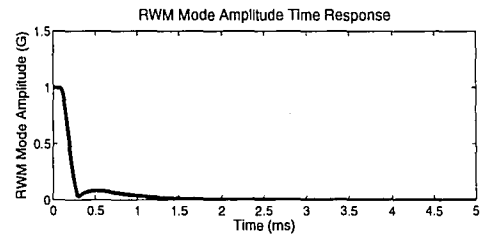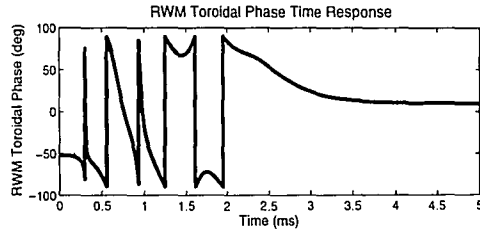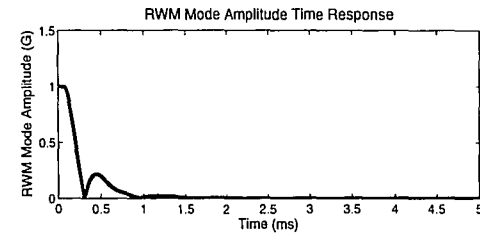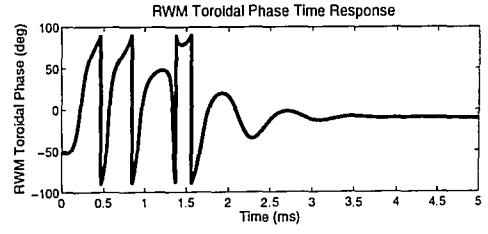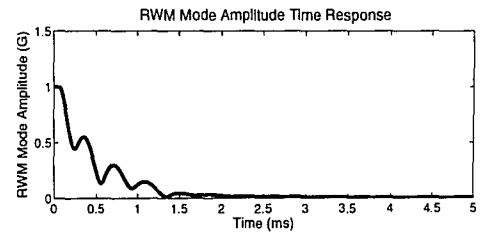Figure 4.10: RWM initial condition response to (a) ramping γ rad/s for (b) LQG, (c) LQRY, (d) NCF, (e) DK, and (f) PD.

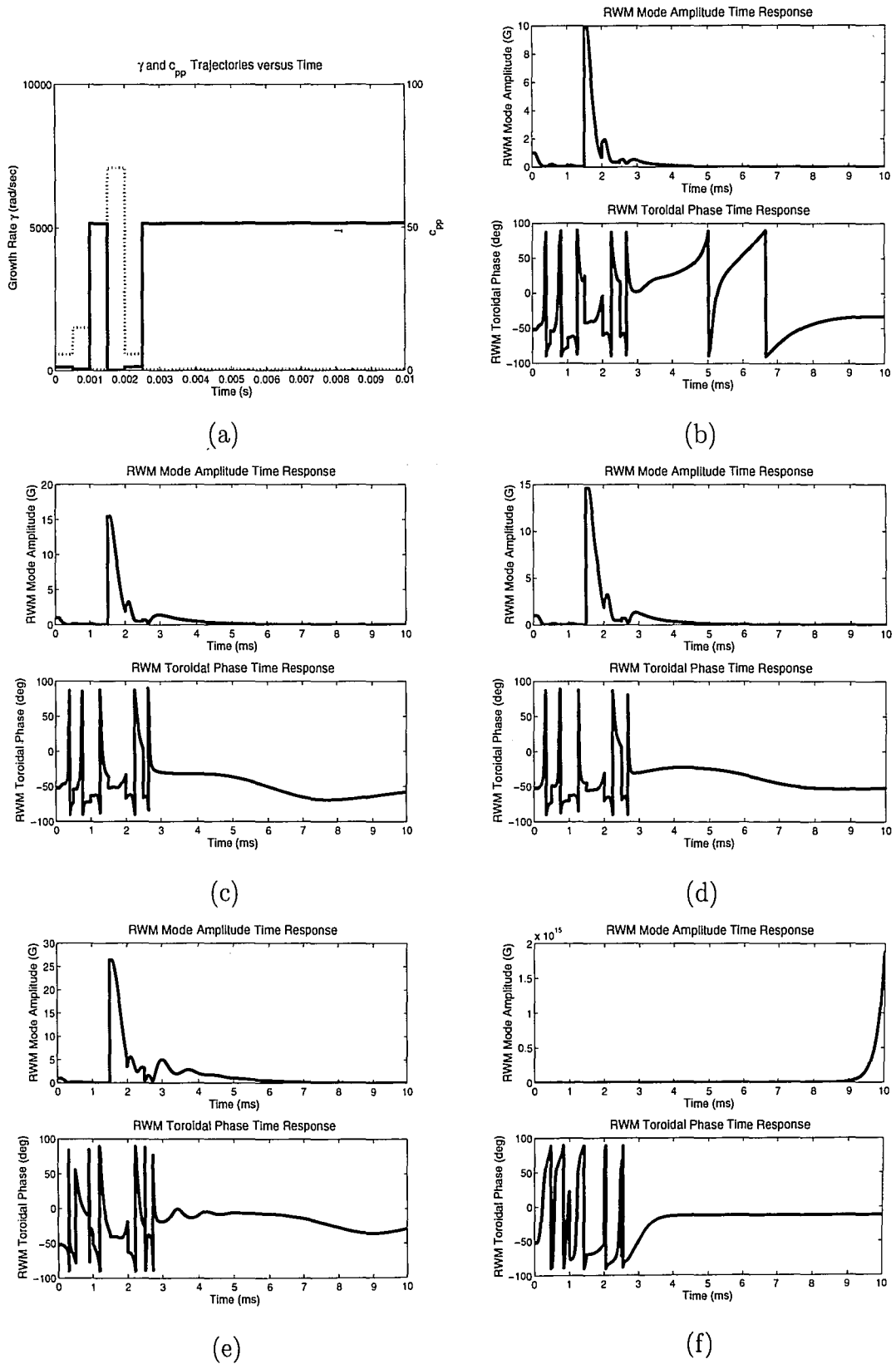Figure 4.11: RWM initial condition response to (a) stepping γ rad/s for (b) LQG, (c) LQRY, (d) NCF, (e) DK, and (f) PD.
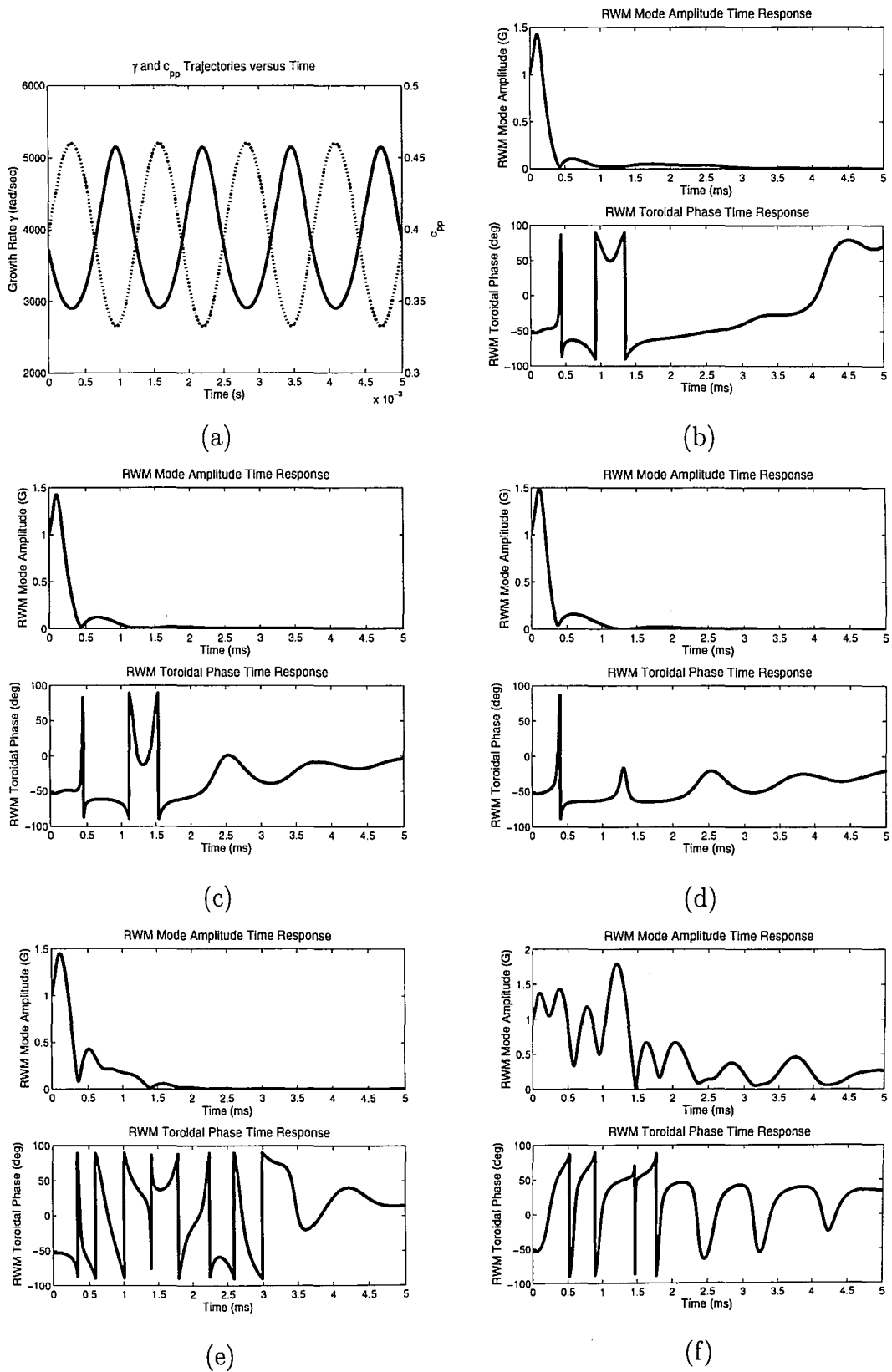
Figure 4.12: RWM initial condition response to (a) sinusoidal γ rad/s for (b) LQG, (c) LQRY, (d) NCF, (e) DK, and (f) PD.
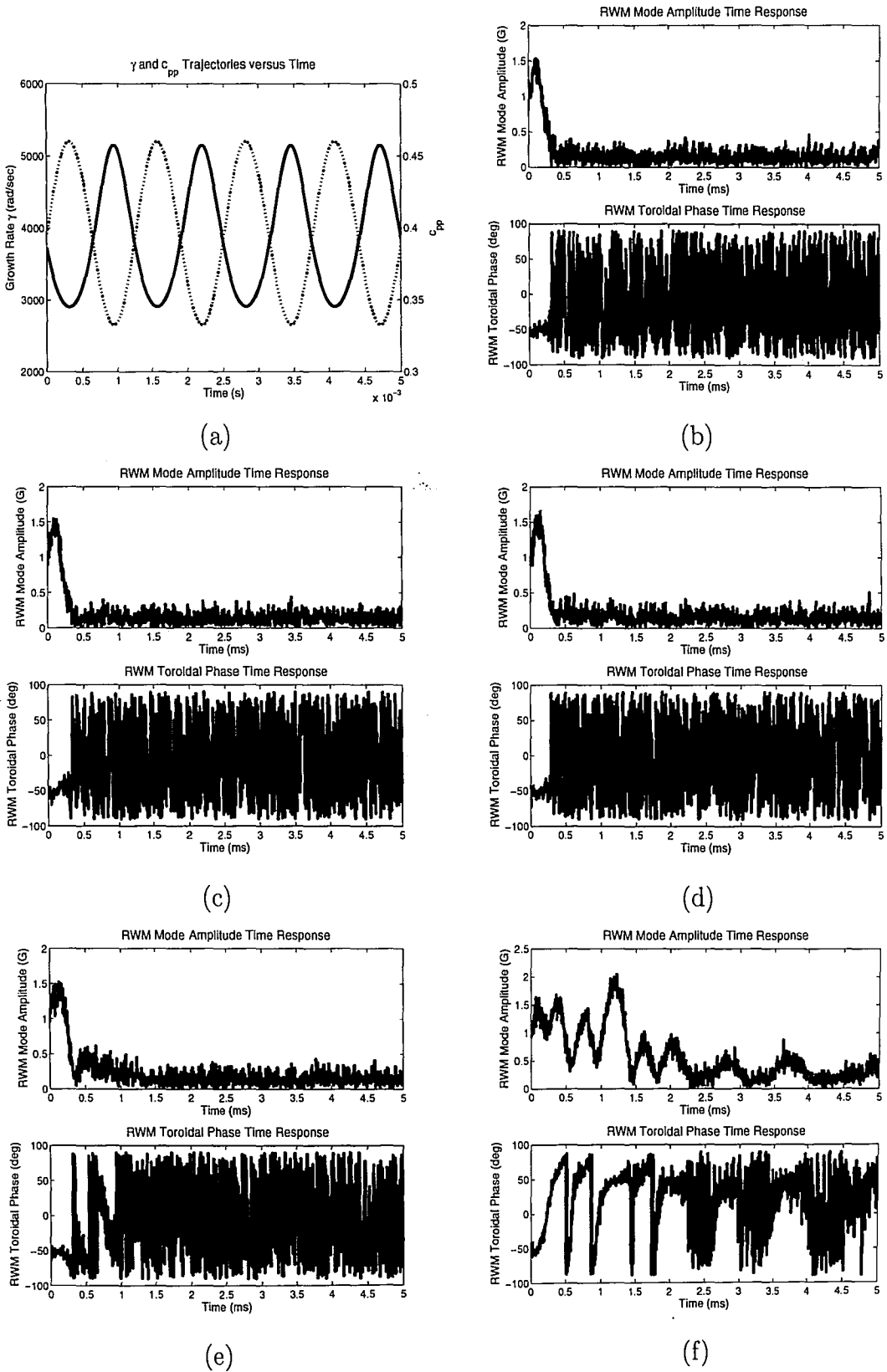
Figure 4.13: RWM initial condition response to (a) sinusoidal γ rad/s with 0.15 G RMS noise for (b) LQG, (c) LQRY, (d) NCF, (e) DK, and (f) PD.

Chapter 5

Conclusion and Future Works

5.1 Conclusion

A toroidal current sheet model for the DIII-D tokamak plasma was restructured into a robust control framework, isolating the RWM growth rate γ (c_{pp}), the key term of RWM instability. With the system model in this framework, the DK-iteration method was applied to develop a structured-singular-value-based robust controller for a pre-determined range of γ. Since the plasma RWM growth rate can vary throughout the operation of the DIII-D tokamak, the design of a controller that can stabilize the system over the entire physical range of γ is critical.

Four other controller designs were considered (LQG, $LQRY$, NCF, and PD) and compared with the robust parametric DK controller. Through simulations and reported stability and performance ranges, the effectiveness of each controller was quantified. An extensive sweep of PD gains allowed for a superior PD controller compared to previously reported values [13].

Despite the improvement in the PD controller, the stability and performance ranges are limited. The LQG provides the widest range of stability and the smallest order controller of the model based controllers. The NCF has the widest performance

range. The *DK* controller's stability and performance ranges are slightly narrower than the other model based controllers, however the range without saturating the control coils is wider and it can withstand more noise than the other controllers. The optimal controller choice depends on the importance of each of these tradeoffs. In terms of robust stability, the model based controller could eliminate the need of online identification and controller scheduling.

5.2   Future Works

While synthesizing the *DK* controller the algorithm used assumes that the uncertain parameter is complex. Since in the case of the RWM model the uncertain parameter is real, using a *DK*-iteration based on complex uncertainty is not conservative enough. Since the phase information is known through the real uncertainty, better results could be achieved using a modified algorithm, the *DGK*-iteration [14].

Although a robust controller can be designed to handle a range of RWM growth rates, adaptive control techniques are still worth investigating. Using the toroidal current sheet model, a transformation into the discrete-time state space representation was described. This transformation can be used to assist the development of a system identification algorithm, which can provide real-time online parameter estimation of the c_{pp} variable. A discrete-time identification algorithm for state space systems can be found in [15]. Once the system identification algorithm can identify c_{pp} parameter, adaptive control techniques can be implemented to provide stabilizing effects on the resistive wall mode.

Bibliography

[1] Pironti A. and Walker M.L., "Fusion, Tokamaks, and Plasma Control," *IEEE Control Systems Magazine*, v 25, n 5, October 2005, p.30-43.

[2] Walker M.L., Humphreys D.A. *et al.*, "Emerging Applications in Tokamak Plasma Control," *IEEE Control Systems Magazine*, v 26, n 2, April 2006, p.35-61.

[3] Strait E.J., Bialek J. *et al.*, "Resistive wall stabilization of high-beta plasmas in DIII-D," *Nucl. Fusion* **43**, 2003, p.434.

[4] Edgell D.H., Kim J.S. *et al.*, "Magnetohydrodynamic mode identification from magnetic probe signals via a matched filter method," *Rev. Sci. Instrum.*, v 73, n 4, April 2002, p 1761.

[5] Humphreys D.A., Garofalo A. *et al.*, "RWM Sheet Current Plasma Response Model, *Engineering Physics Memo*, No. EPM010129a, January 29, 2001.

[6] In Y., *et al*, "Model-based dynamic resistive wall mode identification and feedback control in the DIII-D tokamak," *Phys. Plasmas*, v 13, n 6, June 2006, p 62512-1-12.

[7] Kailath T., *Linear Systems*, Prentice-Hall, 1979.

[8] Strait E.J., Bialek J.M. *et al.*, "Resistive wall mode stabilization with internal feedback coils in DIII-D," *Phys. Plasmas* **11**, 2004, p.2505.

[9] Packard A.K., *What's new with μ: Structured uncertainty in multivariable control*, Ph.D. Thesis, University of California at Berkeley, 1988.

[10] Zhou K., Doyle J.C., and Glover K., *Robust and Optimal Control*, Prentice Hall, 1996.

[11] Skogestad S. and Postlethwaite I., *Multivariable Feedback Control; Analysis and Design*, Wiley, 2005.

[12] McFarlane, D.C., and K. Glover, "Robust Controller Design using Normalised Coprime Factor Plant Descriptions", Springer Verlag, Berlin, Germany,*Lecture Notes in Control and Information Sciences*, vol. 138, 1989.

[13] Blair J.A., *Comparison of Potential Approaches for Resistive Wall Mode Stabilization Based on Plasma Eigenmode Model*, M.Sc. Thesis, Lehigh University, 2006.

[14] Young P.M. *Controller Design with Real Parametric Uncertainty*, Technical Memorandum No. CIT-CDS 93-016, California Institute of Technology, 1993.

[15] Ljung L. and S. Söderström. *Theory and Practice of Recursive Identification.* Cambridge: MIT Press, 1983. p122-130.

Vita

Joseph Dalessio, son of Fred and Arlene Dalessio, was born in Aston, Pennsylvania on October 3, 1984. He attended and received his Bachelor of Science in Mechanical Engineering from Lehigh University in May 2006. He also received a Minor in Aerospace Engineering from Lehigh University in December 2006. Joseph was awarded the Presidential Scholarship, Robert C. Watson Memorial Scholarship, Biddle A. Whigham Scholarship, and the 2006 Alan Stenning Award. He is a member of Tau Beta Pi Engineering Honors Fraternity and Pi Tau Sigma Honors Fraternity. In 2007 he worked at Lehigh University toward his MSc. degree with Prof. E. Schuster in the Laboratory for Control of Complex Physical Systems. Upon the accomplishment of Master Degree he will work in the Life Sciences and Chemical Analysis department of Agilent Technologies.

Referred Conferences

J. Dalessio, E. Schuster, D.A. Humphreys, M.L. Walker, Y. In, and J.S. Kim, "Robust Control of Resistive Wall Modes in Tokamak Plasmas using μ-synthesis," Proceedings of the *49th American Physical Society Annual Meeting of the Division of Plasma Physics*, Orlando, FL, USA, November 2007.

Submitted Papers

J. Dalessio, E. Schuster, D.A. Humphreys, M.L. Walker, Y. In, and J.S. Kim, "Robust Control of Resistive Wall Modes in Tokamak Plasmas using μ-synthesis," Proceedings of the *17th IFAC World Congress on Automation Control*, Seoul, Korea, July 2008.

C. Xu, J. Dalessio, Y. Ou, E. Schuster, T.C. Luce, J.R. Ferron, M.L. Walker and D.A. Humphreys, "POD-Based Optimal Control of Current Profile in Tokamak Plasmas via Nonlinear Programming," Proceedings of the *2008 American Control Conference*, Seattle, WA, USA, June 2008.

END OF TITLE